Voltage-dependent modulation of elastic moduli in lattice metamaterials: Emergence of a programmable state-transition capability

A. Singh[a], T. Mukhopadhyay[b,*], S. Adhikari[c], B. Bhattacharya[a]

[a]*Department of Mechanical Engineering, Indian Institute of Technology Kanpur, Kanpur, India*
[b]*Department of Aerospace Engineering, Indian Institute of Technology Kanpur, Kanpur, India*
[c]*College of Engineering, Swansea University, Swansea, UK*

Abstract

Two-dimensional lattices are ideal candidate for developing artificially engineered materials and structures across different length-scales, leading to unprecedented multi-functional mechanical properties which can not be achieved in naturally occurring materials and systems. Characterization of effective elastic properties of these lattices is essential for their adoption as structural elements of various devices and systems. An enormous amount of research has been conducted on different geometry of lattices to identify and characterize various parameters which affect the elastic properties. However, till date we can not control the elastic properties actively for a lattice microstructure, meaning that the elastic properties of such lattices are not truly programmable. All the parameters that control the effective elastic properties are passive in nature. After manufacturing the lattice structure with a certain set of geometric or material-based parameters, there is no room to modulate the properties further. In this article, we propose a hybrid lattice micro-structure by integrating piezo-electric materials with the members of the lattice for active voltage-dependent modulation of elastic properties. A bottom-up multi-physics based analytical framework leading to closed-form formulae is derived for hexagonal lattices to demonstrate the concept of active lattices. It is noticed that the Young's moduli are voltage-dependent, while the shear modulus and the Poisson's ratios are not functions of the applied voltage. Thus, the compound mechanics of deformation induced by external mechanical stresses and electric field lead to an active control over the Young's moduli as a function of voltage. Interestingly, it turns out that a programmable state-transition of the Young's moduli from positive to negative values with a wide range can be achieved in such hybrid lattices. The physics-based analytical framework for active modulation of voltage-dependent elastic properties on the basis of operational demands provide the necessary physical insights and confidence for potential practical exploitation of the proposed concept in various futuristic multi-functional structural systems and devices across different length-scales.

Keywords: Active honeycombs, Elastic properties of lattices, Negative Young's modulus, Hybrid piezoelectric honeycomb, Multi-physical lattice microstructures

*Corresponding author: Tanmoy Mukhopadhyay (ORCID id: https://orcid.org/0000-0002-0778-6515)
Email addresses: `amangill@iitk.ac.in` (A. Singh), `tanmoy@iitk.ac.in` (T. Mukhopadhyay),
`S.Adhikari@swansea.ac.uk` (S. Adhikari), `bishakh@iitk.ac.in` (B. Bhattacharya)

Nomenclature

α Piezoelectric beam to substrate beam thickness ratio.

$\bar{\epsilon}_{33}^s$ Permittivity at constant strain.

δ Total displacement.

δ_σ Displacement due to externally applied stress.

δ_p Displacement due to piezoelectric material.

ϵ_1 Strain in direction X or direction 1.

ϵ_2 Strain in direction Y or direction 2.

ϵ_{33}^T Permittivity at constant stress.

γ Shear strain.

κ Piezoelectric beam to substrate beam Young's modulus ratio.

ν_{12}, ν_{21} Poisson's ratio.

ϕ Angle of rotation.

σ_1 Stress applied in direction X or direction 1.

σ_2 Stress applied in direction Y or direction 2.

τ Shear stress.

$[A_q]$ Shape function matrix.

$[K]$ Stiffness matrix.

$\{D\}$ Vector of electric displacement components.

$\{E\}$ Vector of electric field components.

$\{F\}$ Force generated due to piezoelectric material under the influence of voltage.

$\{q\}$ Displacement vector.

$\{S\}$ Engineering strain.

θ Cell angle.

θ_{CR} Critical cell angle

$\tilde{E}_1$, $\tilde{E}_2$, $\tilde{G}_{12}$ Non-dimensional elastic moduli.

A_p Area of piezoelectric beam.

A_s Area of substrate beam.

B_p Voltage and extension coupling component.

C_p — Internal capacitance of piezoelectric material.

d_{31} — Piezoelectric Constant.

E_1 — Young's modulus of the honeycomb structure in direction X or direction 1.

E_2 — Young's modulus of the honeycomb structure in direction Y or direction 2.

e_{31} — Effective piezoelectric stress constant.

E_3 — Electric Field.

F_s — Shear force.

G_{12} — In-plane shear modulus.

h — Length of vertical cell wall.

H_p — First moment of area of piezoelectric beam.

H_s — First moment of area of substrate beam.

I_p — Second moment of area of piezoelectric beam.

I_s — Second moment of area of substrate beam.

J_p — Voltage and curvature coupling component.

L — Length of slant cell wall.

M — Moment generated due to externally applied stress.

M_p — Moment generated due to piezoelectric material.

P — Load generated due to the application of stress σ_1

s_{11}^E — Elastic compliance at constant electric field.

T_p — Thickness of piezoelectric beam.

T_s — Thickness of substrate beam.

U — Potential Energy.

u — Axial displacement of the beam.

u^0 — Axial displacement of neutral axis at any point x.

u_s — Shear deflection.

V — Applied voltage.

V^s, V^p — Substrate and piezoelectric beam's volume.

W — Load generated due to the application of stress σ_2

w — Transverse displacement of the beam.

w^0 Transverse displacement of neutral axis at any point x.

W_{ie} Internal electrical energy.

W_p Width of piezoelectric beam.

W_s Width of substrate beam.

w_x Rotation of the beam about y axis.

Y_p Young's modulus of piezoelectric beam.

Y_s Young's modulus of substrate beam.

$\{T^s\}$, $\{T^p\}$ Engineering stress in substrate and piezoelectric beam.

1. Introduction

Two-dimensional lattice structural forms can be found in various natural and artificial systems across different length-scales. Such lattices are ideal for developing application-specific multi-functional material microstructures, which are commonly referred as mechanical metamaterials. Lightweight lattice structures with high specific stiffness along with other multi-functional features have gained significant attention over the recent years. 2D lattices can have different shapes such as square, triangular, hexagonal, Kagome, N- Kagome, star triangular honeycomb and mixed (square and Kagome) (Zhang et al., 2008; Wei et al., 2020). Neverthless, out of all these shapes, the most common and widely-adopted shape is the honeycomb structure, which can offer high strength to weight ratio (Zenkert, 1995) and geometry-dependent simultaneous modulation capability of different elastic moduli (like Young's modulus, shear modulus and Poisson's ratios), shock absorption, high-temperature processing properties, fatigue strength and acoustic properties (Ryvkin and Shraga, 2018; Gibson and Ashby, 1999; Jang and Kyriakides, 2015; Sorohan et al., 2019; Wilbert et al., 2011). In this context, it may be noted that such micro-structure dependent material microstructures with periodic forms, which can meet the multi-functional demands of modern structures at different length-scale, are often referred as metamaterials (Mukhopadhyay et al., 2020c; Wang et al., 2020; Mukhopadhyay et al., 2020a; Mukhopadhyay and Adhikari, 2017b). However, elastic properties are one of the most crucial features of such lattice microstructures to characterize their viability for structural application.

A lot of research has been conducted to obtain the equivalent in-plane properties of the regular honeycomb structure (Zhang and Ashby, 1992; El-Sayed et al., 1979; Gibson and Ashby, 1999). Recently, analytical formulations have been developed to find the equivalent in-plane elastic properties for irregular honeycomb and auxetic lattices structures (Mukhopadhyay and Adhikari, 2016a; Zhu et al., 2001) including the effect of viscoelasticity (Mukhopadhyay et al., 2019c). Malek and Gibson (2015) studied the elastic behaviour of periodic hexagon honeycombs analytically and numerically for a wide range of relative densities and cell geometries. Mukhopadhyay and Adhikari (2016c) developed analytical expressions for the effective out-of-plane elastic properties of irregular honeycombs and presented their application in the vibration analysis of sandwich structures. Scarpa et al. (2000) conducted numerical and experimental studies for the change in Poisson's ratios and Young's moduli of honeycomb structures having different geometric arrangements such as cell angle, relative thickness and side cell aspect ratio. Thomas and Tiwari (2019) found that energy absorption and peak crushing force increases with the increase in cell wall thickness whereas a reverse effect was observed as the cell size increases. Effect of non-periodic microstructure on elastic properties of 2D honeycomb was studied by Silva et al. (1995), wherein it was observed that variation in the cell walls leads to a change of 4-9% in elastic constants. The effect on compressive strength of the honeycomb for non-periodic structure with defects was studied by Silva and Gibson (1997). Wang and McDowell (2003) investigated the effect of absent or broken cell walls on in-plane properties by using finite element analysis and found out that some in-plane properties diminish sharply while the other properties decrease gradually as the defect density increases. Mukhopadhyay et al. (2019a) studied the dependency of elastic moduli on vibration frequency and found that except the Poisson ratio, all other properties increase significantly with the increase in frequency. Chen et al. (1999) studied the effect of different types of imperfection such as cell-size variation, cell- wall misalignments, fractured cell walls, missing cells, waviness and non-uniform cell wall thickness on the mechanical properties of honeycombs. Mukhopadhyay and Adhikari (2016b, 2017a) reported through an analytical framework that the presence of quasi-random structural and material irregularity in lattice materials could lead to a significant level of variation in the effective elastic moduli. The mechanics-based analysis of hexagonal lattice-like structures has been extended to nano-scale for analysing the elastic properties of graphene and
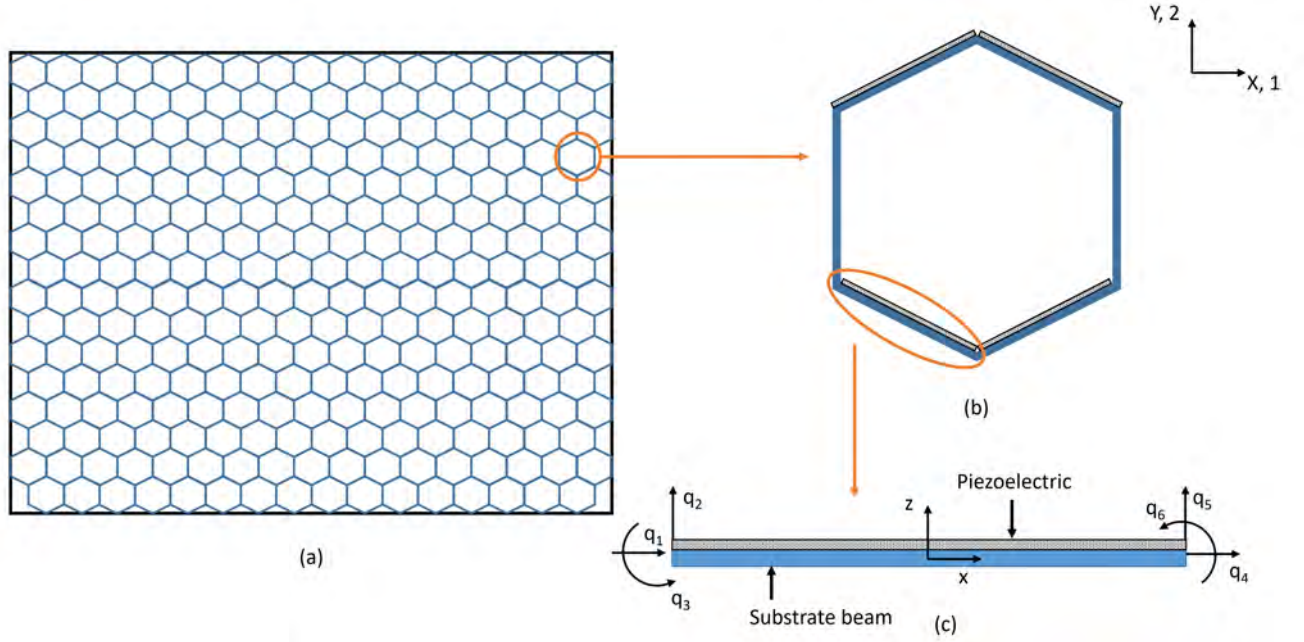
Fig. 1: (a) Typical representation of a regular honeycomb lattice structure in XY plane (global coordinates) (b) Detailed microstructure of a single honeycomb unit cell with piezoelectric patches over inclined cell walls (the vertical members do not have any piezoelectric patches) (c) Degree of freedoms for a single cell wall (i.e. beam) having piezo patch. Note that the analytical formulation in this article is derived following a bottom-up framework, wherein we start by analysing an active piezo-embedded beam and thereafter utilize the stiffness matrix of a single beam to characterize the deformation behaviour of a unit cell. Since the entire lattice under consideration is perfectly periodic, we can obtain the global behaviour of the entire lattice (such as effective elastic properties) based on deformation analysis of a single unit cell. Here the analytical formulation for an individual beam has been derived considering the local coordinate system (x, z) as shown in subfigure(c), where the direction x is along the beam length. The in-plane global axis system is considered as X-Y (or, 1-2 to represent the elastic moduli), as shown in subfigure (b).

other 2D materials (Mukhopadhyay et al., 2017a,b, 2020b). Rapaka et al. (2020) found out that due to the presence of defects the dynamic performance of honeycomb deteriorates as the value of impact velocity increases . Balawi and Abot (2008) performed an experimental study to observe the dependency of in-plane properties of honeycomb over a wide range of relative density and found that the existing models give close results for low relative density, and not for high relative densities. This observation makes sense since most of the existing deformation models of honeycombs rely on Euler-Bernoulli beam theories. Grima et al. (2011) proposed an improved analytical model from a practical view-point by showing the importance of considering thickness of ribs, which was missing in most of the existing models. Zhao et al. (2020) studied the effect of large deformation on the in-plane properties and found that these properties do not remain constant, hence changes with the change in strain. Harkati et al. (2020) studied the effect of internal angle and curvature of the cell walls and concluded that elastic moduli decreases as the radius of curvature increases.

A critical review of the existing literature on elastic properties of honeycombs reveals that most of the developments so far lead to a passive property. This means that the elastic moduli are dependent on the microstructural geometry and intrinsic material properties of the lattice. The elastic moduli in such lattices are not truly programmable, i.e. it is not possible to modulate the elastic properties in a single lattice once it is manufactured. In this article, we aim to propose a hybrid lattice microstructure by integrating piezo-electric materials (Dwivedi et al., 2020; Crawley and Anderson, 1990) with the members of the lattice for active voltage-dependent modulation

of elastic properties. A multi-physics based analytical framework leading to closed-form formulae will be derived for hexagonal lattices to demonstrate the concept of active lattices. The compound mechanics of deformation induced by external stresses and electric field will be exploited to achieve an active control over the Young's moduli as a function of voltage. This paper also aims to stretch further for exploring the possibility of programmable state transition of the Young's moduli from positive to negative values with a wide range in such hybrid lattices.

We would adopt a multi-step bottom-up analytical derivation approach to establish the closed-form expressions for elastic moduli of active honeycomb lattices as shown in Fig. 1. The fundamental idea behind the proposed active network of beams lies on the principle that the effective deformation behaviour of a piezo-embedded beam would be governed by two components, mechanical deformation due to externally applied stress and electric-field induced deformation. Since the nature of deformation by these two components are independent of each other depending on applied tensile or compressive stresses and positive or negative applied voltage, the effective deformation of the beam, and thereby the global behaviour of the entire lattice, would be a function of the applied stress and voltage. We start by analysing an active piezo-embedded beam (refer to Fig. 1(c)) and thereafter utilize the stiffness matrix of a single beam to characterize the deformation behaviour of a unit cell. Since the entire lattice under consideration is perfectly periodic, we can obtain the global behaviour of the entire lattice (such as effective elastic properties) based on deformation analysis of a single unit cell. The article hereafter is organized in the order of chronological development as follows, section 2: derivation of the deformation mechanics for piezo-embedded composite beams under an applied voltage, section 3: a unit cell based approach to establish the closed-form formulae of the hybrid lattice using the deformation mechanics of individual beam elements, section 4: results and discussion to demonstrate the effect of multiphysical (such as voltage and mechanical stress) and microstructural parameters (i.e. geometry and material properties) and section 5: conclusion and perspective.

2. Analytical formulation for voltage-dependent deformation behaviour of piezo embedded hybrid beams

In this section we derive the deformation mechanics of an individual piezo-embedded beam element under the application of voltage. It may be noted in this context that piezoelectric materials are widely known for their sensing, actuation, vibration control and energy harvesting related applications (Dwivedi et al., 2020; Crawley and de Luist, 1987; Lee et al., 2004; Iyer et al., 2016; Li et al., 2017; Chen et al., 2017). In order to model the beams, different mathematical theories for bending and extension (such as uniform strain and Euler-Bernoulli) have been proposed (Crawley and Anderson, 1990). In the following subsections, we provide the derivation of the mathematical relationship for voltage-dependent deformation behaviour of piezo-embedded hybrid beams, followed by numerical validations with existing literature.

2.1. Derivation of stiffness matrix of a cell wall

A beam having d_{31} (i.e. when electric field is applied in direction 3, induced strain develops in direction 1) piezoelectric patch(es) attached on its surface (unimorph/bimorph) is considered, as shown in Fig. 1. The formulation given below is independent of unimorph and bimorph configuration. The displacement of the beam can be represented as (Erturk and Inman, 2011)

$$u(x, z, t) = u^0(x, t) - z w^0_{,x}(x, t) \tag{1}$$

$$w(x, t) = w^0(x, t) \tag{2}$$

where $u^0(x,t)$ and $w^0(x,t)$ are the displacements of the neutral axis at any point x and time t in the axial and the transverse direction. Total potential energy of the structure is the sum of the potential energy of the substrate beam and the piezoelectric layers and can be written as

$$U = \frac{1}{2} \left(\int_{V_s} \{S\}^t \{T^s\} dV_s + \int_{V_p} \{S\}^t \{T^p\} dV_p \right) \tag{3}$$

where, S is engineering strain, T is engineering stress, and s and p in subscript and superscript stand for substrate and piezoelectric material, respectively. The volume for the each of the material is obtained by integrating over the individual volumes (V). Here, t in superscript indicates transpose (otherwise time). The strain in x direction is

$$S_{11}(x,z,t) = \frac{\partial u^0(x,t)}{\partial x} - z \frac{\partial^2 w^0(x,t)}{\partial x^2} \tag{4}$$

The substrate is assumed to be isotropic hence, obeys the hook's law

$$T_{11}^s(x,z,t) = Y_s S_{11}(x,z,t) \tag{5}$$

Here elastic modulus of the substrate layer is represented by Y_s. Stress component in the piezo-electric material can be calculated as

$$T_{11}^p(x,z,t) = Y_p S_{11} - \bar{e}_{31} E_3 = Y_p S_{11}(x,z,t) + \bar{e}_{31} \frac{V}{T_p} \tag{6}$$

Here, $E_3(t) = -\frac{V}{T_p}$ i.e. electric field can be written as function of voltage where, voltage across the electrodes is denoted by V, piezoelectric material thickness is T_p and permittivity constant, elastic modulus, piezoelectric stress constant are given as $\bar{\epsilon}_{33}^s = \epsilon_{33}^T - \frac{(d_{31})^2}{s_{11}^E}$, $Y_p = \frac{1}{s_{11}^E}$, $\bar{e}_{31} = \frac{d_{31}}{s_{11}^E}$, respectively. Substituting all the above defined values in Equation (3) we get

$$
\begin{aligned}
U = \frac{1}{2} \int_0^L \Bigg\{ & Y_s \left[A_s \left(\frac{\partial u^0(x,t)}{\partial x} \right)^2 + I_s \left(\frac{\partial^2 w^0(x,t)}{\partial x^2} \right)^2 - 2H_s \left(\frac{\partial u^0(x,t)}{\partial x} \frac{\partial^2 w^0(x,t)}{\partial x^2} \right) \right] \\
& + Y_p \left[A_p \left(\frac{\partial u^0(x,t)}{\partial x} \right)^2 + I_p \left(\frac{\partial^2 w^0(x,t)}{\partial x^2} \right)^2 - 2H_p \left(\frac{\partial u^0(x,t)}{\partial x} \frac{\partial^2 w^0(x,t)}{\partial x^2} \right) \right] \\
& + B_p V \frac{\partial u^0(x,t)}{\partial x} - J_p V \frac{\partial^2 w^0(x,t)}{\partial x^2} \Bigg\} dx
\end{aligned}
\tag{7}
$$

Here, $A_s, H_s, I_s, A_p, H_p, I_p, B_p, J_p$ are given as (for any arbitrary point x)

$$(A_s, H_s, I_s) = \iint_s \left(1, z, z^2 \right) dy dz \tag{8}$$

$$(A_p, H_p, I_p) = \iint_p \left(1, z, z^2 \right) dy dz \tag{9}$$

$$B_p = \iint_p \frac{\bar{e}_{31}}{T_p} dy dz \tag{10}$$

$$J_p = \iint_p \frac{\bar{e}_{31}}{T_p} z \, dy \, dz \tag{11}$$

For a symmetric structure like bimorph or any symmetric multimorph H_s and H_p are equal to zero. Coupling of voltage and extensional component is given by B_p, whereas J_p gives the coupling for voltage and the curvature component.

The internal electrical energy in the piezoelectric layer can be written as (Erturk and Inman, 2011)

$$W_{ie} = \frac{1}{2} \int_{V_p} \{E\}^t \{D\} dV_p = -\frac{1}{2} \int_0^L \left\{ B_p V \frac{\partial u^0(x,t)}{\partial x} - J_p V \frac{\partial^2 w^0(x,t)}{\partial x^2} \right\} dx + \frac{1}{2} C_p V^2 \tag{12}$$

Here, value of C_p is

$$C_p = \bar{\epsilon}_{33}^s \frac{A_p}{T_p} \tag{13}$$

Considering a two noded beam element with three degrees of freedom (i.e. axial, transverse and rotation) having a scaled length of 1, displacement vector q can be written as

$$\{q\} = \{u_1 \ w_1 \ w_{x1} \ u_2 \ w_2 \ w_{x2}\}^t \tag{14}$$

The values of u^0 and w^0 can be obtained from the relations given below

$$\begin{Bmatrix} u^0 \\ w^0 \end{Bmatrix} = \begin{bmatrix} F_1 & 0 & 0 & F_2 & 0 & 0 \\ 0 & H_1 & H_2 & 0 & H_3 & H_4 \end{bmatrix} \{q\} \tag{15}$$

$$u^0 = \{1 \ \ 0\}[A_q]\{q\} \tag{16}$$

$$w^0 = \{1 \ \ 0\}[A_q]\{q\} \tag{17}$$

Shape functions are given as

$$F_1 = 1 - \xi \tag{18a}$$
$$F_2 = \xi \tag{18b}$$
$$H_1 = 1 - 3\xi^2 + 2\xi^3 \tag{18c}$$
$$H_2 = L\left(\xi - 2\xi^2 + \xi^3\right) \tag{18d}$$
$$H_3 = 3\xi^2 - 2\xi^3 \tag{18e}$$
$$H_4 = L\left(-\xi^2 + \xi^3\right) \tag{18f}$$

Here, $\xi = \dfrac{x}{L}$. In short, the above equations can also be written as

$$u^0 = \{n_1\}[A_q]\{q\} \tag{19}$$

$$w^0 = \{n_2\}[A_q]\{q\} \tag{20}$$

Taking variational and differentiating Equation (19) and Equation (20) we get

$$\delta u^0_{,x} = \{B_1\}_{,x}\{\delta q\} \tag{21}$$

$$\delta w^0_{,xx} = \{B_2\}_{,xx}\{\delta q\} \tag{22}$$

The value of $\{B_1\}$ and $\{B_2\}$ in Equation (21) and Equation (22) are

$$\{B_1\} = \{n_1\}[A_q] \tag{23}$$

$$\{B_2\} = \{n_2\}[A_q] \tag{24}$$

Taking the variational (keeping the voltage constant, as we want to deform the structure and hold it at a particular position, i.e not vibrating it) of the potential energy from Equation (3) and the internal energy from Equation (12), followed by substituting the values we get the following relationships.

$$\delta U = \{\delta q\}^t \Big[(Y_s A_s + Y_p A_p)[M_{11}] + (Y_s I_s + Y_p I_p)[M_{22}] - (Y_s H_s + Y_p H_p)[M_{12}]$$
$$- (Y_s H_s + Y_p H_p)[M_{21}] \Big] \{q\} + \{\psi\} \tag{25}$$

The constants mentioned in Equation (25) are as follows

$$[M_{11}] = \int_0^L \{B_1\}_{,x}^t \{B_1\}_{,x} dx, \; [M_{22}] = \int_0^L \{B_2\}_{,xx}^t \{B_2\}_{,xx} dx, \; [M_{12}] = \int_0^L \{B_1\}_{,x}^t \{B_2\}_{,xx} dx,$$

$$[M_{21}] = \int_0^L \{B_2\}_{,xx}^t \{B_1\}_{,x} dx, \; \{\psi_1\} = \int_0^L \frac{1}{2} B_p V \{B_1\}_{,x}^t dx, \; \{\psi_2\} = \int_0^L \frac{1}{2} J_p V \{B_2\}_{,xx}^t dx, \tag{26}$$

$$\{\psi\} = \{\psi_1\} - \{\psi_2\}$$

We can rewrite the Equation (25) as

$$\delta U = \{\delta q\}^t \{[K]\{q\} + \{\psi\}\} \tag{27}$$

The value of $[K]$ in Equation (27) is

$$[K] = \Big[(Y_s A_s + Y_p A_p)[M_{11}] + (Y_s I_s + Y_p I_p)[M_{22}] - (Y_s H_s + Y_p H_p)[M_{12}]$$
$$- (Y_s H_s + Y_p H_p)[M_{21}] \Big] \tag{28}$$

For internal energy we get

$$\delta W_{ie} = -\{\delta q\}^t \{\psi\} \tag{29}$$

From Hamilton's principle we have

$$\int_{t_1}^{t_2} (\delta U - \delta W) dt = 0 \tag{30}$$

As we have obtained the expressions of δU and δW_{ie}, substituting them in the Hamilton's principle we get

$$\int_{t_1}^{t_2} \{\delta q\}^t \{[K]\{q\} + 2\{\psi\}\} dt = \{0\} \tag{31}$$

The final form of equilibrium equation can be written as

$$[K]\{q\} + 2\{\psi\} = \{0\} \quad \text{or} \quad [K]\{q\} = \{F\} \tag{32}$$

Value of $\{F\}$ in Equation (32) is given as

$$\{F\} = -2\{\psi\} \tag{33}$$

Subsequently, displacements of a beam due to change in the voltage can be calculated by solving the following equation

$$\{q\}_{6\times 1} = [K]^{-1}_{6\times 6}\{F\}_{6\times 1} \tag{34}$$

The beam has been assumed to be a cantilever beam which is fixed at node 1 and implies that u_1, w_1 and w_{x1} are equal to zero. The expressions of force vector $\{F\}$ and stiffness matrix $[K]$ are

$$\{F\} = \{B_p V \quad 0 \quad -J_p V \quad -B_p V \quad 0 \quad J_p V\}^t \tag{35}$$

$$[K] = \begin{bmatrix} A & 0 & -B & -A & 0 & B \\ 0 & 12C & 6CL & 0 & -12C & 6CL \\ -B & 6CL & 4CL^2 & B & -6CL & 2CL^2 \\ -A & 0 & B & A & 0 & -B \\ 0 & -12C & -6CL & 0 & 12C & -6CL \\ B & 6CL & 2CL^2 & -B & -6CL & 4CL^2 \end{bmatrix} \tag{36}$$

The values of A, B and C are given as

$$A = \frac{Y_p A_p + Y_s A_s}{L} \tag{37}$$

$$B = \frac{Y_p H_p + Y_s H_s}{L} \tag{38}$$

$$C = \frac{Y_p I_p + Y_s I_s}{L^3} \tag{39}$$

The values of the dimensional constants like A_p, A_s, H_p, H_s, I_p and I_s are discussed in the following section.

2.2. Determination of the constants

The constants which have been used in the formulation provided in the preceding subsection are given below. The detailed view and the integration limits used to obtain the constants are taken from neutral axis, which has been assumed to be at the center of the beam (refer to Fig. 2).
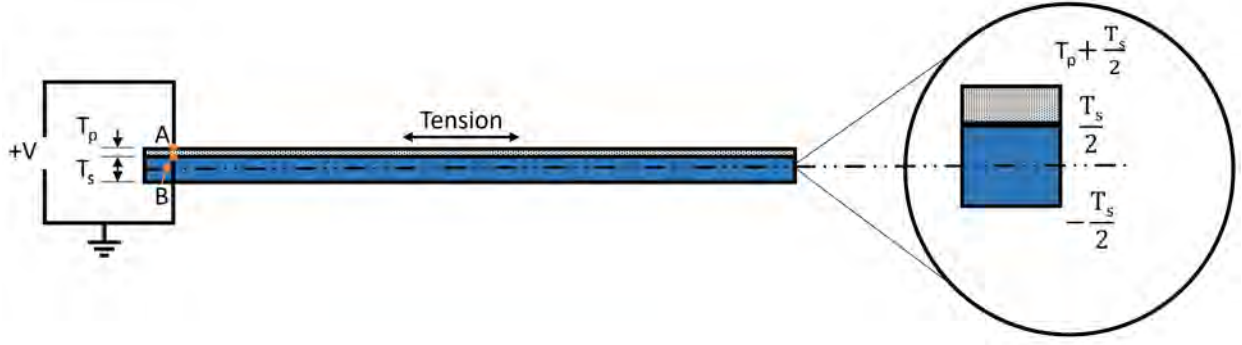
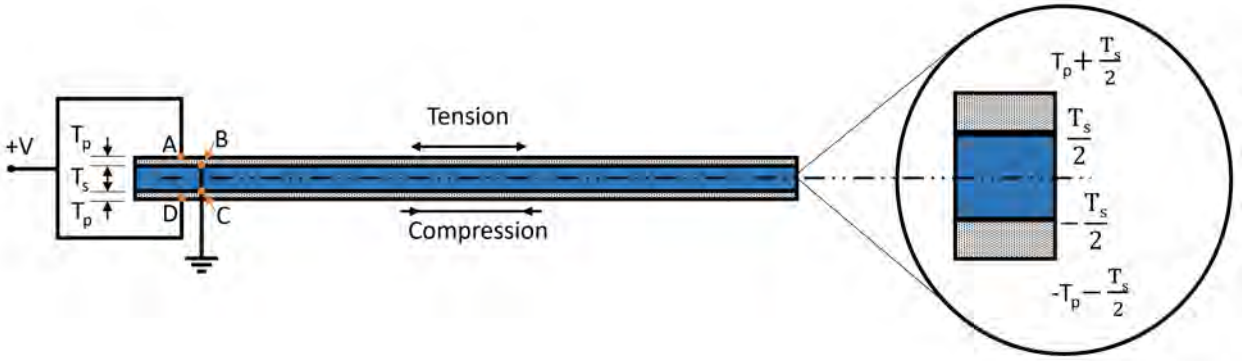### 2.2.1. Substrate beam

Area of beam is given as

$$A_s = \int\limits_0^{W_s} \int\limits_{-\frac{T_s}{2}}^{\frac{T_s}{2}} dy dz = W_s T_s \tag{40}$$

First moment of area is given as

$$H_s = \int\limits_0^{W_s} \int\limits_{-\frac{T_s}{2}}^{\frac{T_s}{2}} z dy dz = \frac{W_s}{2}\left(\left(\frac{T_s}{2}\right)^2 - \left(\frac{T_s}{2}\right)^2\right) = 0 \tag{41}$$

(a) Unimorph

(b) Bimorph

Fig. 2: Unimorph and bimorph beam configurations showing the integration limits from the neutral axis (which is assumed to be at the geometric center of the substrate). Electrical connectivity of the piezo layers are also indicated in the figures.

Second moment of area is given as

$$I_s = \int\limits_{0}^{W_s} \int\limits_{-\frac{T_s}{2}}^{\frac{T_s}{2}} z^2 dydz = \frac{W_s}{3}\left(\left(\frac{T_s}{2}\right)^3 - \left(-\frac{T_s}{2}\right)^3\right) = \frac{W_s T_s^3}{12} \tag{42}$$

2.2.2. Piezo layer in unimorph configuration

Area of piezoelectric beam is given as

$$A_p = \int\limits_{0}^{W_p} \int\limits_{\frac{T_s}{2}}^{\frac{T_s}{2}+T_p} dydz = W_p T_p \tag{43}$$

First moment of area is given as

$$H_p = \int\limits_{0}^{W_p} \int\limits_{\frac{T_s}{2}}^{\frac{T_s}{2}+T_p} z dydz = \frac{W_p}{2}(T_s T_p + T_p^2) \tag{44}$$

Second moment of area is given as

$$I_p = \int\limits_0^{W_p} \int\limits_{\frac{T_s}{2}}^{\frac{T_s}{2}+T_p} z^2 dy dz = \frac{W_p}{3}\left(T_p^3 + \frac{3}{2}T_p^2 T_s + \frac{3}{4}T_p T_s^2\right) \tag{45}$$

Piezoelectric coupling terms are given as

$$B_p = \int\limits_0^{W_p} \int\limits_{\frac{T_s}{2}}^{\frac{T_s}{2}+T_p} \frac{e_{31}}{T_p} dy dz = W_p e_{31} \tag{46}$$

$$J_p = \int\limits_0^{W_p} \int\limits_{\frac{T_s}{2}}^{\frac{T_s}{2}+T_p} \frac{e_{31}}{T_p} z dy dz = \frac{W_p e_{31}}{2T_p}(T_s T_p + T_p^2) \tag{47}$$

2.2.3. Piezo layer in bimorph configuration
Area of piezoelectric beam is given as

$$A_p = \int\limits_0^{W_p} \int\limits_{\frac{T_s}{2}}^{\frac{T_s}{2}+T_p} dy dz + \int\limits_0^{W_p} \int\limits_{\frac{-T_s}{2}-T_p}^{-\frac{T_s}{2}} dy dz = 2W_p T_p \tag{48}$$

First moment of area is given as

$$H_p = \int\limits_0^{W_p} \int\limits_{\frac{T_s}{2}}^{\frac{T_s}{2}+T_p} z dy dz + \int\limits_0^{W_p} \int\limits_{\frac{-T_s}{2}-T_p}^{-\frac{T_s}{2}} z dy dz = 0 \tag{49}$$

Second moment of area is given as

$$I_p = \int\limits_0^{W_p} \int\limits_{\frac{T_s}{2}}^{\frac{T_s}{2}+T_p} z^2 dy dz + \int\limits_0^{W_p} \int\limits_{\frac{-T_s}{2}-T_p}^{-\frac{T_s}{2}} z^2 dy dz = \frac{2W_p}{3}\left(T_p + \frac{T_s}{2}\right)^3 - \frac{W_p T_s^3}{12} \tag{50}$$

Piezoelectric coupling terms are given as

$$B_p = \int\limits_0^{W_p} \int\limits_{\frac{T_s}{2}}^{\frac{T_s}{2}+T_p} \frac{e_{31}}{T_p} dy dz + \int\limits_0^{W_p} \int\limits_{\frac{-T_s}{2}-T_p}^{-\frac{T_s}{2}} \frac{e_{31}}{T_p} dy dz = 2W_p e_{31} \tag{51}$$

$$J_p = \int\limits_0^{W_p} \int\limits_{\frac{T_s}{2}}^{\frac{T_s}{2}+T_p} \frac{e_{31}}{T_p} z dy dz + \int\limits_0^{W_p} \int\limits_{\frac{-T_s}{2}-T_p}^{-\frac{T_s}{2}} \frac{e_{31}}{T_p} z dy dz = \frac{W_p e_{31}}{T_p}\left(\left(T_p + \frac{T_s}{2}\right)^2 - \left(\frac{T_s}{2}\right)^2\right) \tag{52}$$

For bimorph configuration, the values of $J_{p,\text{bottom}}$ and $J_{p,\text{top}}$ add only under one condition, i.e. when the top piezoelectric beam is in tension and the bottom piezoelectric beam is in compression. This will only happen, when top and bottom beams are supplied with equal but opposite polarity voltages as shown in Figure 2(*b*). Hence, the deformation due to both the piezoelectric beams is of

same nature. So, under these conditions value of J_p for top and bottom beam adds to each other, and the final value of J_p having a positive sign is obtained for the above mentioned connections and voltage polarity. If the polarity of the voltage is reversed the sign of J_p is also reversed. If voltage having the same polarity is applied to both the top and bottom beam, then the value of J_p goes to zero.

2.3. Validation with existing literature

The stiffness matrix that we obtained in the previous section is of the order 6×6. Here neglecting the axial deformation and considering only the vertical deformation and rotation, the matrix is reduced to a 4×4. We use this stiffness matrix to obtain the deformation of a cantilever beam and compare the result with literature for validation. The dimensions and material properties used for validation are given in Table 1. A comparison of the obtained voltage-dependent displacements based on the current stiffness matrix with the Euler-Bernoulli beam model (Chopra and Sirohi, 2013) is shown in Fig. 3. The results are obtained for a cantilever beam (i.e. one end of the beam is fixed and the other end is free) using the stiffness matrix of a single beam element (with two nodes and three degrees of freedom at each node) as derived in subsection 2.1. It can be observed that the displacements are in good agreement, corroborating the accuracy and validity of the voltage-dependent stiffness matrix derived in the preceding section. It gives us adequate confidence to use the stiffness matrix of an individual beam element for deriving the effective elastic properties of the entire lattice based on a unit cell, as presented in the following section. These analytical expressions can be implemented in different scenarios (Chopra and Sirohi, 2013; Erturk and Inman, 2011), such as: 1. Length and width of the piezoelectric beam can be equal to or less than that of the substrate beam, 2. Thickness of the piezoelectric beam can be more or less than the substrate beam (satisfying Euler Bernoulli beam assumptions) 3. For bimorph configurations, both parallel (as shown in Figure 2(b)) and series connections can be analysed.

Table 1: Dimensions and material properties used for validating the response of a single beam.

Parameter	Dimensions
Piezo length(mm)	20
Piezo Width (mm)	200×10^{-3}
Piezo Thickness (mm)	50×10^{-3}
Piezo Constant d_{31} (m/V)	-2.74×10^{-10}
Young's Modulus of Piezo (N/m^2)	1.27×10^{11}
Beam Length (mm)	20
Beam Width (mm)	200×10^{-3}
Beam Thickness (mm)	100×10^{-3}
Young's Modulus of Beam (N/m^2)	70×10^{9}

3. Effective voltage-dependent elastic moduli of hexagonal lattices

We use the voltage-dependent stiffness matrix of an individual beam element to derive the effective voltage-dependent elastic properties of the entire lattice. A unit cell based approach is adopted for this purpose, as shown in Fig. 1(b). Out of the six-cell walls, piezoelectric materials are attached on the inclined cellular walls only since it is well documented that the Young's moduli and Poisson's ratios (ν_{12} and ν_{21}) are dependent only on the deformation behaviour of these inclined
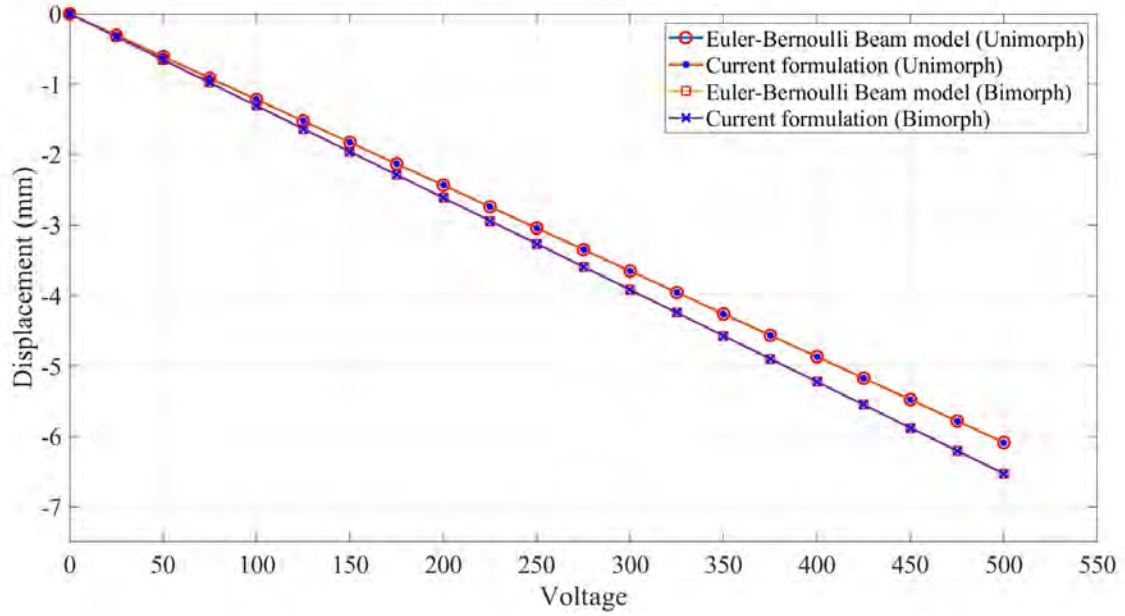
Fig. 3: Current voltage-dependent stiffness model and Euler-Bernoulli beam model comparison for displacement of a cantilever beam having unimorph and bimorph configurations, where the loading is due to variation of voltage only (Validation of the stiffness matrix for an individual beam with existing literature).

cell walls in case of thin-walled honeycombs with high axial rigidity (Gibson and Ashby, 1999). The applied piezo patches could have two configurations, unimorph and bimorph (refer to Fig. 2). The voltage on the piezo patch is applied in such a manner that two adjacent inclined members deflect in the same direction. For the bimorph, configuration voltage is applied in such a way that the deflection of the beam occurs due to pure bending only. The effect of voltage on the in-plane elastic properties can be captured by subjecting the unit cell under combined influence of external loading and voltage. For longitudinal Young's modulus and ν_{12} stress (σ_1) is applied in direction 1 as shown in Fig. 4 whereas, for transverse Young's modulus and ν_{21} stress (σ_2) is applied in direction 2 as shown in Fig. 5. The shear force τ is applied to obtain the expression for G_{12} as shown in Fig. 6.

For deriving the in-plane elastic properties, we obtain the expressions for different components of strains under the application of external mechanical stresses as discussed in the preceding paragraph. The final expressions of the elastic moduli depend on either the relevant strain components only (for Poisson's ratios) or both the relevant stress and strain components (for Young's and shear moduli). Normally, when the deformation of the constituting beam members are not voltage dependent (or $V = 0$ in the current active microstructural configuration), the strain components of a unit cell are a function of the geometry of the unit cell, intrinsic elastic moduli (i.e. the material properties of the beam member) and the applied stress component. However, in case of the proposed hybrid unit cell under voltage-dependent deformation of the constituting beams, the compound effect of two deformation mechanisms (induced by applied stresses and applied electric field) controls the effective deformation of the individual beams. Subsequently, the strain components of a unit cell have two parts, the first component being induced by applied stresses (similar to the case of passive material, or for $V = 0$ in piezo-electric material) and the second component is induced due to applied electrical field. Thus in the newly proposed framework, effective strain of a unit cell is a function of the geometry of the unit cell, intrinsic elastic moduli (i.e. the material properties of the beam member), applied external stress and electrical field (i.e. voltage). This makes it possible to actively modulate the effective elastic properties of the proposed lattice using

programmable electrical field. The voltage-dependent expressions of elastic moduli derived in this section are valid for both tensile and compressive loading as well as for both polarities of voltage under small deformation.

In general, for the derivation of the two Young's moduli and the two Poisson's ratios, the vertical members can contribute by means of axial deformation only when direction of the required deformation and the direction of applied stress are parallel to the vertical members (note that the lattice structure under consideration consists of symmetric and regular unit cells). In such regular symmetric lattices, there is no possibility of bending deformation in the calculation of Young's moduli and Poisson's ratios for the vertical members since the stresses are either applied in perpendicular (note that equal forces act in the same direction at the two ends of a vertical member) or parallel directions to the axis of the vertical members. In the derivation of in-plane shear modulus, both the bending and axial deformation of the vertical members could contribute. However, it is widely accepted in the literature that the contribution of axial deformation of the vertical members in the total deformation of a hexagonal unit cell is negligible compared to bending deformation of the members. This becomes more predominant in most of the small-deformation based analyses where it is also a standard practice to consider the beam-like members to be axially rigid. Hence longitudinal deformation of such beam members does not contribute to the total deformation of the entire honeycomb structure significantly for any of the derivations of in-plane elastic moduli considered in the current article. Moreover, with the assumption of very less wall thickness of the honeycomb cells ($\frac{T}{L} \sim 10^{-2}$, where T is the total thickness of the piezo layer and substrate beam, while L represent the length of the beam), the contribution of shear deformation is neglected (Mukhopadhyay and Adhikari, 2016b). It may be noted that since the above conditions are valid for a majority of the industry-grade honeycomb structures with low specific density (i.e. low cell wall thickness), similar assumption has been widely adopted in the literature (Gibson and Ashby, 1999).

3.1. Longitudinal Young's modulus E_1

The following derivation for E_1 is based on free body diagram of the lattice unit cell as shown in Fig. 4. In the derivation of E_1, the stress is applied in X-direction and the total deformation is also obtained in the X-direction. For the analysis of a unit cell, equivalent forces are applied at the four joints of the unit cell which are located at the two ends of each of the vertical members. Since these forces are equal in magnitude and they act in a direction perpendicular to the axes of the vertical members, there is no scope of these vertical members to contribute in the total deformation of the unit cell in X-direction through axial or bending deformations. Thus, under the application of stress in X-direction, the two vertical members in a unit cell move relative to each other due to the deformation of the slant members, while maintaining their relative parallel directions. For this reason, the vertical members do not contribute in the derivation of E_1 directly. However, length of the vertical members does appear in the expression of E_1.

A stress σ_1 is applied in the longitudinal direction for deriving the expression of E_1 (Gibson and Ashby, 1999). It produces bending of the inclined member having length L. An additional bending is produced by the end moments which come into play as we apply the external voltage to the whole structure. The combined effect of external stress and externally applied voltage determines the displacement of the cell walls as given in Equation (56). In order to maintain equilibrium, force N_1 has to be zero. The cell walls have a thickness of $T_{\text{total}} = T_s + nT_p$ (T_s and T_p represent the thickness of the substrate beam and a piezo layer respectively, $n = 1$ for unimorph and $n = 2$ for bimorph), depth of the beam substrate (W_s) and piezo layers (W_p) have been assumed to be equal and same as the thickness of the honeycomb panel in the out-of-plane direction. Other dimensions
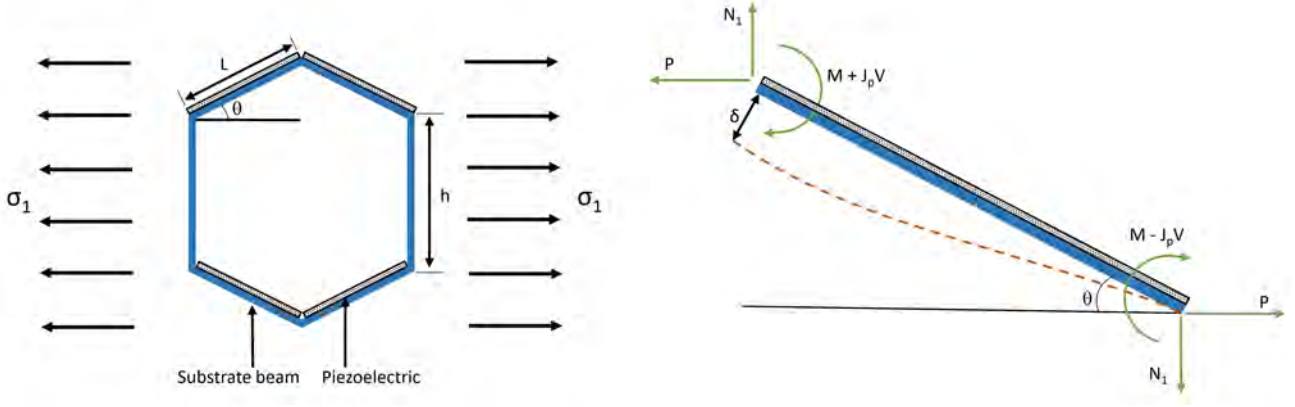
Fig. 4: Single honeycomb unit under the application of stress in direction X and free-body diagram of the slant member which is used in the analysis for E_1.

of the honeycomb unit cell are shown in Fig. 4. We present the derivation of E_1 considering two different cases of unimorph and bimorph configurations in the following subsections.

3.1.1. E_1 for unimorph configuration

The moment M is given as

$$M = \frac{PL\sin\theta}{2} \tag{53}$$

Load P (generated due to the application of stress σ_1) can be given as

$$P = \sigma_1 \left(h + L\sin\theta\right) W_s \tag{54}$$

The above expression is written based on the periodic nature of the lattice under consideration. For deriving the expression of E_1, the edge of a lattice perpendicular to the X-direction needs to be considered. In the X-direction, it can be assumed that the forces caused by the applied stress is lumped at the joints wherein contribution of every pair of adjacent vertical and slant members can be lumped at the points joining these two members. The moment M_p due to piezoelectric material is obtained from the stiffness matrix as

$$M_p = J_p V \tag{55}$$

From the standard beam theory (Roark and Young, 1976), total displacement due to the above mentioned moment components can be expressed as

$$\delta = \delta_{\sigma_1} + \delta_p = \frac{P\sin\theta L^3}{12EI_{\text{total}}} + \frac{J_p V}{2CL} \tag{56}$$

Here C is $\dfrac{Y_p I_p + Y_s I_s}{L^3}$, where Y is Young's modulus and I is second moment of area (p and s stand for piezo and substrate beam respectively). J_p is given as $\dfrac{W_p e_{31}\left(T_p^2 + T_p T_s\right)}{2T_p}$ and $EI_{\text{total}} = Y_p I_p + Y_s I_s$. The component of deflection in X direction is $\delta\sin\theta$, thus, the strain in X-direction can be given as

$$\epsilon_1 = \frac{\delta\sin\theta}{L\cos\theta} \tag{57}$$

Young's modulus in X-direction for unimorph configuration is given as

$$E_1 = Y_s \left(\frac{T_s}{L}\right)^3 \frac{\cos\theta}{\sin^2\theta \left(\frac{h}{L} + \sin\theta\right)} \left(\frac{1 + 4\kappa \left[\alpha^3 + 1.5\alpha^2 + 0.75\alpha\right]}{1 + A_{uni}}\right) \tag{58}$$

Here, the value of A_{uni} is

$$A_{uni} = \left(\frac{d_{31} Y_p V}{\sigma_1 L \left(\frac{h}{L} + \sin\theta\right)}\right) \left(\frac{3(1 + \alpha)}{\sin\theta}\right) \left(\frac{T_s}{L}\right) \tag{59}$$

In the above expression following parameters have been used, $T_p = \alpha T_s$, $\kappa = \dfrac{Y_p}{Y_s}$.

3.1.2. E_1 for bimorph configuration

For the bimorph configuration, all expressions remain same as the unimorph configuration, except second moment of area (I_p) and J_p, as shown in Equation (50) and Equation (52), respectively. Subsequently, E_1 for the bimorph configuration can be expressed as

$$E_1 = Y_s \left(\frac{T_s}{L}\right)^3 \frac{\cos\theta}{\sin^2\theta \left(\frac{h}{L} + \sin\theta\right)} \left(\frac{1 + 8\kappa \left[\alpha^3 + 1.5\alpha^2 + 0.75\alpha\right]}{1 + A_{Bi}}\right) \tag{60}$$

Here, the value of A_{Bi} is

$$A_{Bi} = \left(\frac{d_{31} Y_p V}{\sigma_1 L \left(\frac{h}{L} + \sin\theta\right)}\right) \left(\frac{6(1 + \alpha)}{\sin\theta}\right) \left(\frac{T_s}{L}\right) \tag{61}$$

3.2. Transverse Young's modulus E_2

Stress σ_2 is applied in direction Y to derive the transverse Young's modulus E_2, as shown in Fig. 5. In order to maintain equilibrium, force N_2 has to be zero. The effective deflection of a single unit is due to the bending of the inclined cell walls under the combined effect of external stress and voltage induced moments, similar to the case of E_1.

3.2.1. E_2 for unimorph configuration

The moment M is given as

$$M = \frac{WL\cos\theta}{2} \tag{62}$$

The value of load W (generated due to the application of stress σ_2) applied in direction 2 is

$$W = \sigma_2 L W_s \cos\theta \tag{63}$$

The moment due to piezoelectric material M_p is obtained from the stiffness matrix as

$$M_p = J_p V \tag{64}$$

Total deflection of the slant member under the loading as shown in Fig. 5

$$\delta = \delta_{\sigma_2} + \delta_p = \frac{WL^3 \cos\theta}{12EI_{\text{total}}} + \frac{J_p V}{2CL} \tag{65}$$
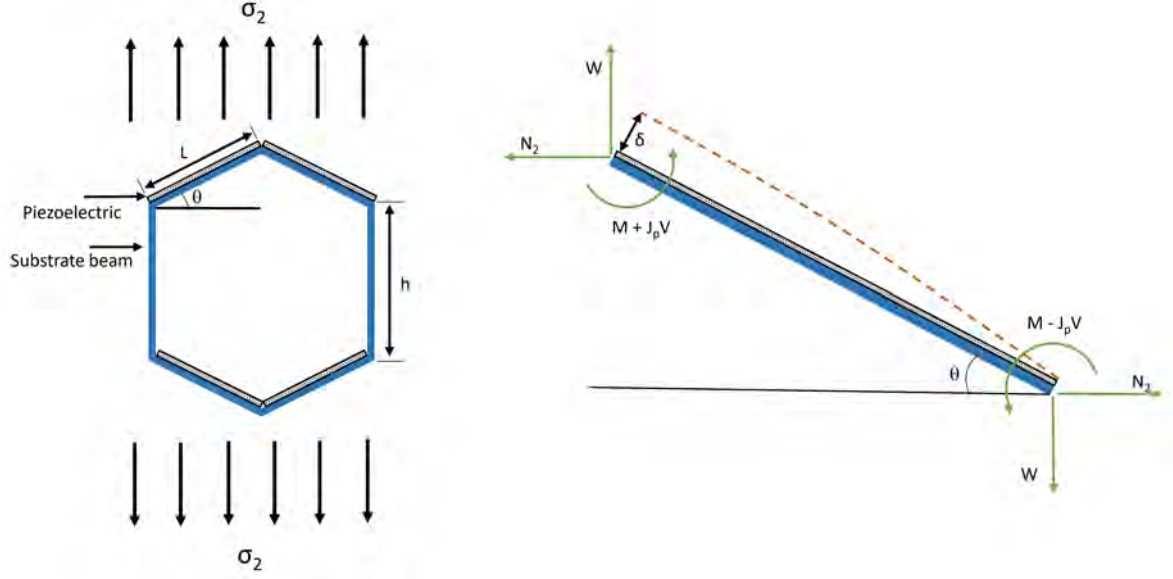
Fig. 5: Single honeycomb unit under the application of stress in direction Y and free-body diagram of the slant member which is used in the analysis for E_2.

The component of the deflection in Y direction is $\delta \cos \theta$. Subsequently, total strain in Y direction can be given as

$$\epsilon_2 = \frac{\delta \cos \theta}{(h + L \sin \theta)} \tag{66}$$

Young's Modulus in transverse direction E_2 for unimorph configuration can be expressed as

$$E_2 = \frac{\sigma_2}{\epsilon_2} \tag{67}$$

Thus we get the final expression for E_2 in case of unimorph configuration as

$$E_2 = Y_s \left(\frac{T_s}{L}\right)^3 \frac{\left(\dfrac{h}{L} + \sin \theta\right)}{\cos^3 \theta} \left(\frac{1 + 4\kappa \left[\alpha^3 + 1.5\alpha^2 + 0.75\alpha\right]}{1 + B_{uni}}\right) \tag{68}$$

The value of B_{uni} is

$$B_{uni} = \left(\frac{d_{31} Y_p V}{\sigma_2 L}\right) \left(\frac{3(1 + \alpha)}{\cos^2 \theta}\right) \left(\frac{T_s}{L}\right) \tag{69}$$

3.2.2. E_2 for bimorph configuration

For bimorph configuration all expressions remain same except I_p and J_p, which are given in Equation (50) and Equation (52), respectively. Thus E_2 for bimorph configuration can be expressed as

$$E_2 = Y_s \left(\frac{T_s}{L}\right)^3 \frac{\left(\dfrac{h}{L} + \sin \theta\right)}{\cos^3 \theta} \left(\frac{1 + 8\kappa \left[\alpha^3 + 1.5\alpha^2 + 0.75\alpha\right]}{1 + B_{Bi}}\right) \tag{70}$$

The value of B_{Bi} is

$$B_{Bi} = \left(\frac{d_{31} Y_p V}{\sigma_2 L}\right) \left(\frac{6(1 + \alpha)}{\cos^2 \theta}\right) \left(\frac{T_s}{L}\right) \tag{71}$$

3.3. Poisson's ratio ν_{12}

Poisson's ratio is defined as the negative ratio of strains normal to, and parallel to, the loading direction. Poisson's ratio ν_{12} can be obtained under loading in direction X as

$$\nu_{12} = -\frac{\epsilon_2}{\epsilon_1} \tag{72}$$

where ϵ_1 and ϵ_2 represent the strains in direction X and direction Y respectively, under the loading in direction X.

Value of ϵ_1 can be obtained from Equation (57) and ϵ_2 can be written as

$$\epsilon_2 = \frac{-\delta \cos\theta}{(h + L\sin\theta)} \tag{73}$$

Expression for Poisson's ratio due to loading in direction X can be expressed as

$$\nu_{12} = \frac{\cos^2\theta}{\left(\dfrac{h}{L} + \sin\theta\right)\sin\theta} \tag{74}$$

From the above expression it is evident that Poisson's ratio ν_{12} is independent of voltage. The expression is the same for unimorph and bimorph configurations.

3.4. Poisson's ratio ν_{21}

Poisson's ratio ν_{21} can be obtained under loading in direction Y as

$$\nu_{21} = -\frac{\epsilon_1}{\epsilon_2} \tag{75}$$

where ϵ_1 and ϵ_2 represent the strains in direction X and direction Y respectively, under the loading in direction Y. The value of ϵ_2 can be obtained from Equation 66 and ϵ_1 can be expressed as

$$\epsilon_1 = -\frac{\delta \sin\theta}{L\cos\theta} \tag{76}$$

Expression for Poisson's ratio due to loading in direction Y can be expressed as

$$\nu_{21} = \frac{\left(\dfrac{h}{L} + \sin\theta\right)\sin\theta}{\cos^2\theta} \tag{77}$$

From the above expression it is evident that Poisson's ratio ν_{21} is also independent of voltage and the above expression is valid for both unimorph and bimorph configurations.

3.5. Shear modulus G_{12}

Shear stress τ is applied to derive the expression for G_{12}, as shown in Fig. 6. Due to symmetry of points A, B and C, they do not have any relative motion during the shearing of the honeycomb. The total shear deflection u_s (deflection of point D in the X direction with respect to the points A and C) is due to the bending of the beam BD and its rotation about the point B by an angle ϕ. As the bending stiffness of the beams, AB and BC are equal, each one of them shares half of the moment M. It is interesting to notice that voltage-dependent moments generated due to piezo in members AB and BC get cancelled by each other. Hence, the effect of voltage in shear deformation of the unit cell (and subsequently in the shear modulus of the lattice) is not present. However, if we attach piezo patches in the vertical members as well (which is not the currently proposed microstructure), the shear modulus would be voltage-dependent. From Fig. 6 expression for moment M can be written as
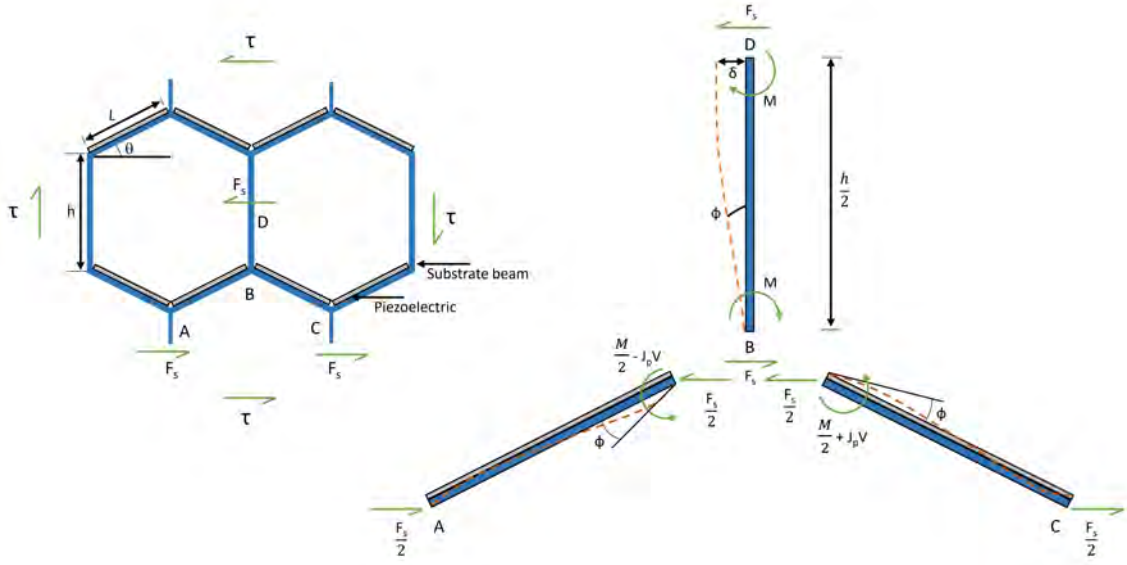
$$M = \frac{F_s h}{4} \tag{78}$$

Fig. 6: Typical representation of honeycomb units under the application of shear stress and the free-body diagrams of three members which are used in the analysis of G_{12}.

Value of F_s is given as

$$F_s = 2\tau L W_s \cos\theta \tag{79}$$

Using the standard result $\delta = \dfrac{ML^2}{6EI_{\text{total}}}$, the angle of rotation is

$$\phi = \frac{ML}{6EI_{\text{total}}} \tag{80}$$

Shear deflection (u_s) of point D with respect to points A and C is

$$u_s = \frac{\phi h}{2} + \frac{F_s}{3EI_{total}}\left(\frac{h}{2}\right)^3 \tag{81}$$

Shear strain γ can be written as

$$\gamma = \frac{2u_s}{(h + L\sin\theta)} \tag{82}$$

The expression for shear modulus of the lattice (for both unimorph and bimorph configuration) can be expressed as

$$G_{12} = \frac{Y_s\left(\dfrac{T_s}{L}\right)^3\left(\dfrac{h}{L} + \sin\theta\right)}{\left(\dfrac{h}{L}\right)^2\left(1 + \dfrac{2h}{L}\right)\cos\theta} \tag{83}$$

From the above expression it is evident that shear modulus G_{12} is independent of voltage.

3.6. Remarks

From the derivation of effective in-plane elastic moduli of the hexagonal lattice with piezo elements attached to the inclined members, as presented in the preceding subsections, it is noticed that the shear modulus and the two in-plane Poisson's ratios are not voltage dependent and the expressions for these moduli exactly match with the existing literature (Gibson and Ashby, 1999).

Two Young's moduli come out to be a function of the applied electric field, meaning these elastic properties can be modulated as a function of voltage. The voltage-dependent Young's moduli also come out to be a function of the applied external stresses (i.e. σ_1 or σ_2) when $V \neq 0$, unlike the case of conventional elastic moduli reported in literature (Gibson and Ashby, 1999). Though it has been reported in literature that the Young's moduli could be strain or stress-dependent for large deformation analysis (Zhao et al., 2020), this is for the first time we show that Young's moduli can also be a function of the applied external stress under the condition of small deformation. As a result, the Young's moduli of the proposed piezo-embedded hybrid lattices depend on the compound effect of external factors like electrical field (i.e. voltage) and mechanical stress along with the microstructural geometry and intrinsic material properties of the constituent members.

It can be noticed from the derived expressions of E_1 and E_2 (for unimorph and bimorph configurations), tend to match with the well-established expressions in literature (Gibson and Ashby, 1999) when $V \to 0$ and $\alpha \to 0$ (refer to Equations (58), (60), (68) and (70)). The proposed expressions of elastic moduli are also found to conform the reciprocal theorem $E_1 \nu_{21} = E_2 \nu_{12}$ for both unimorph and bimorph configurations when $V \to 0$. The above observations concerning the special cases when the derived expressions match with the existing literature and conformation of reciprocal theorem provide an exact analytical validation of the derived expressions in the preceding subsections and adequate confidence to explore numerical results further.

4. Results and discussion

From the analytical expressions of elastic moduli for the piezo-embedded lattice, as presented in the preceding section, it is noticed that the two Young's moduli are voltage-dependent. The in-plane shear modulus and Poisson's ratios are not dependent on the external electrical field (i.e. voltage). Thus, we would concentrate more in this section on the voltage-dependent modulation of the two Young's moduli. The numerical results are presented following three different categories for unimorph and bimorph configurations: I. special cases (when $\alpha = 0$, or $V = 0$), II. voltage dominant, and III. stress dominant (refer to Fig. 7).

4.1. Elastic moduli when $\alpha = 0$, or $V = 0$

We start with presenting the elastic moduli for the case of $\alpha = 0$ (which automatically implies that there is no effect of voltage since no piezo electric material is present in the beam), which means the piezo-embedded hybrid lattice reduces to conventional mono-material thin-walled lattice system (Gibson and Ashby, 1999). Fig. 8(a) shows the variation of five in-plane elastic moduli for all possible values of cell angles including the auxetic configurations. In order to obtain the non-dimensional plot here, the following scale transformation schemes have been used: $\tilde{E}_1 = \dfrac{E_1}{Y_s} \times 10^8$, $\tilde{E}_2 = \dfrac{E_2}{Y_s} \times 10^8$ and $\tilde{G}_{12} = \dfrac{G_{12}}{Y_s} \times 10^9$. For the present analysis (including all derivations throughout this article) only bending deformation has been considered with the assumption of high axial rigidity and small $\dfrac{T_{\text{total}}}{L} (\approx 10^{-3})$ ratio, under which condition the effect due to axial and shear deformations become negligible. Under the assumption of bending dominated deformation of hexagonal lattices, the results become less accurate as the cell angle approaches to zero, when the axial deformation is inevitable to become dominant. The plots shown in Fig. 8(a) (obtained based on the derived formulae for a special case of $\alpha = 0$) matches well with the results presented by Mukhopadhyay and Adhikari (2016a), which necessarily provides a numerical validation for the proposed analytical formulation of this paper.

To present the numerical results in a logical order of development, now we show the effect of having unimorph and bimorph configurations on the elastic properties under the condition of
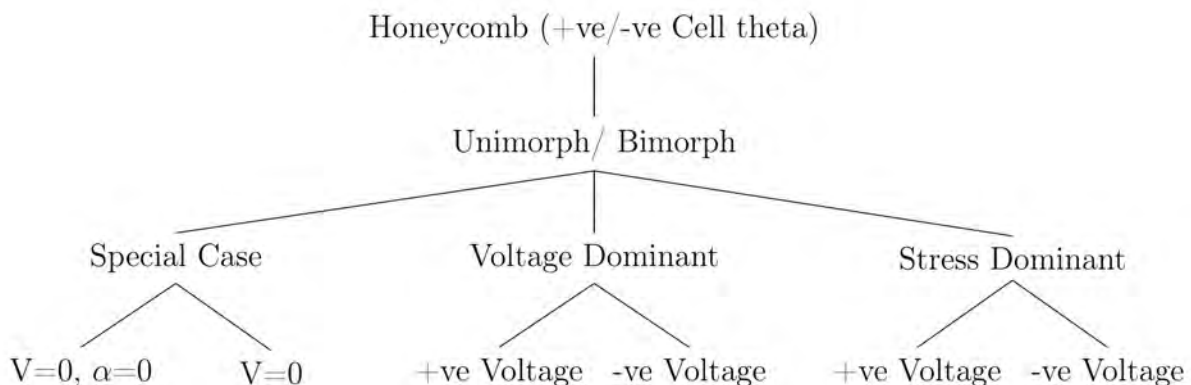
Fig. 7: Branch tree explaining the numerical results presented following three different categories for unimorph and bimorph configurations: I. special cases (when $V = 0$), II. voltage dominant, and III. stress dominant.

$V = 0$ (refer to Fig. 8(b–c)). Such cases are equivalent to having a passive hybrid hexagonal lattice with cell walls composed of bi-layer composites and sandwich structures, respectively. The value of α is considered as 0.5 and κ is 1270, while the voltage is equal to zero. The addition of piezo patches over the cell walls increase their overall thickness for both unimorph and bimorph

Table 2: Parameters that determine the sign for Young's modulus (E_1, E_2).

| d_{31}	Voltage	Cell angle	A_{uni}/A_{Bi}	B_{uni}/B_{Bi}
Negative	Postive	Postive	Negative	Negative
Negative	Postive	Negative	Postive	Negative
Negative	Negative	Postive	Postive	Postive
Negative	Negative	Negative	Negative	Postive

configurations. It can be observed that the value of Young's moduli increase for unimorph and bimorph configurations in comparison to the non-piezo configuration, while a reverse trend is noticed for the shear modulus. This is because of the fact that $\dfrac{T_{\text{total}}}{L}$ ratio is maintained constant for all the three cases. Thus, for unimorph and bimorph configurations, L would increase as a result of higher value of T_{total}. Since h remains constant, the $\dfrac{h}{L}$ ratio decreases with the addition of piezo layers and also constant κ is not present in the shear modulus expression (83). Subsequently, the increasing or decreasing trends of the elastic moduli for unimorph and bimorph configurations can be readily explained based on the closed-form formulae derived in the preceding section.

4.2. Voltage-dependent Young's moduli

In this subsection, we explore the voltage and stress dependent behaviour of the elastic properties of lattice materials. Since, the two Young's moduli are dependent on voltage and externally applied mechanical stress, we focus on these to elastic moduli here. We have considered the voltage in the range of $0 - 400V$, while the applied stress in the range of $25 - 3300Pa$. Since the Young's moduli of a particular lattice microstructure (i.e. for a particular lattice geometry and intrinsic material properties) depends on the compound effect of applied electrical field and external stress, the effect of one of these two parameters may be insignificant when the other parameter assumes an extremely high value. For this reason, with the current aim of this paper to explore the voltage-dependence of Young's moduli, we consider two possible cases: I. voltage dominant
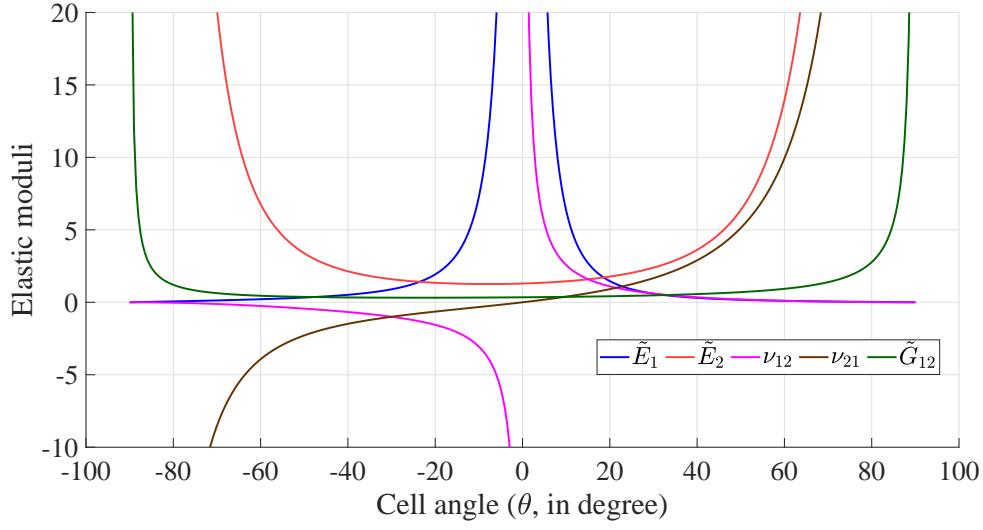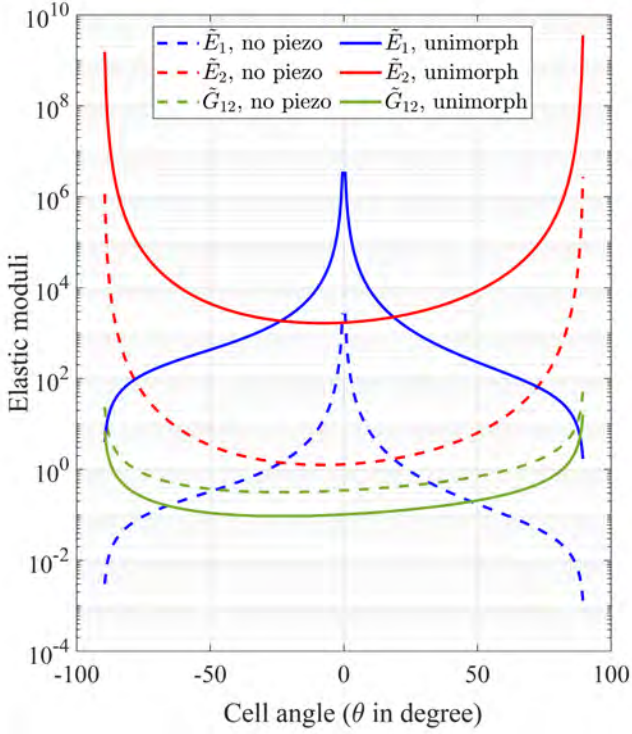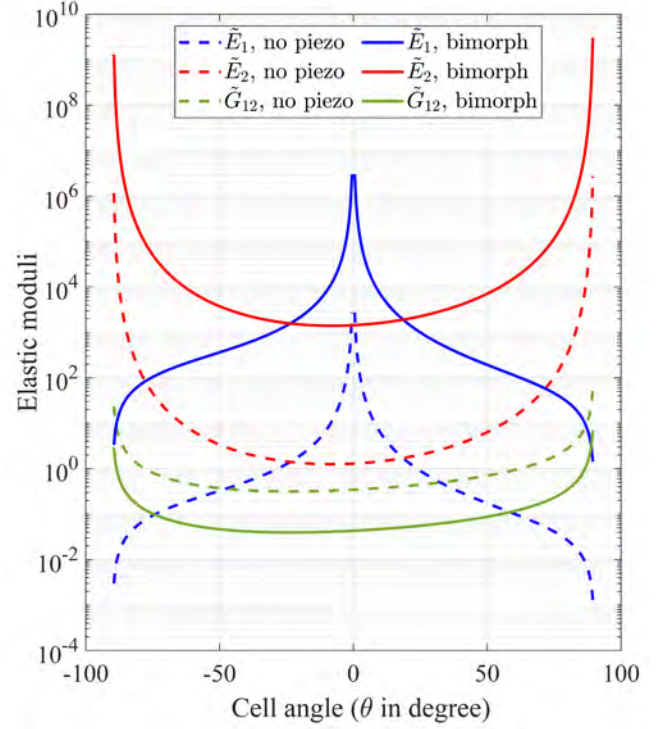
Fig. 8: Elastic moduli of the lattice for the special cases where voltage is zero. (a) Results for unimorph/ bimorph configurations considering $\alpha = 0$ (i.e. piezo thickness is zero) (b) Results for unimorph configurations considering $\alpha = 0.5$ (this configuration is like a composite bi-layer cell wall honeycomb without any active material component) along with comparative results including the case of no piezo patches (c) Results for bimorph configurations considering $\alpha = 0.5$ (this configuration is like a sandwich tri-layer cell wall honeycomb without any active material component) along with comparative results including the case of no piezo patches.

(VD) when the applied stress is less than 60 Pa, II. stress dominant (SD) when the applied stress is more than 1000 Pa. Clearly, the effect of voltage will be more significant in the first case, while that will be somewhat shadowed by the higher stress induced deformation in the second case.
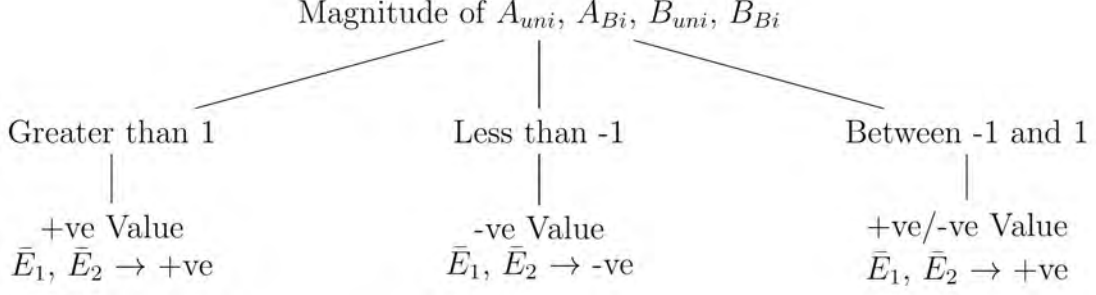
Greater than 1

Less than -1

Between -1 and 1

+ve Value
$\bar{E}_1$, $\bar{E}_2 \rightarrow$ +ve

-ve Value
$\bar{E}_1$, $\bar{E}_2 \rightarrow$ -ve

+ve/-ve Value
$\bar{E}_1$, $\bar{E}_2 \rightarrow$ +ve

Fig. 9: Importance of magnitude of A_{uni}, A_{Bi}, B_{uni} and B_{Bi} to determine the signs of $\bar{E}_1$ and $\bar{E}_2$.

For generality, we have investigated the Young's moduli considering a non-dimensional form hereafter ($\bar{E}_1 = E_1 \setminus Y_s$ and $\bar{E}_2 = E_2 \setminus Y_s$), where we use the notations $\bar{E}_1$ and $\bar{E}_2$ for the non-dimensional Young's modulus in longitudinal and transverse directions respectively. The numerical results for $\bar{E}_1$ and $\bar{E}_2$ considering unimorph and bimorph configurations are presented in Figures 10 – 14, revealing that the Young's moduli are significantly affected by the compound effect of voltage and applied stress. It is interesting to notice from the figures that the compound interaction between these two modulating factors (voltage and applied stress) could lead to unusual negative values of elastic moduli. Though negative Young's moduli in lattice materials have been reported under dynamic conditions (Adhikari et al., 2020; Mukhopadhyay et al., 2019b), this is the first instance where we demonstrate that the Young's moduli could become negative in static condition when an external electrical field is applied. It is shown that a programmable state-transition of Young's moduli (i.e. reversal of sign) can be achieved in a single material microstructure based on the active parameter space. Here by 'state-transition' we refer to the reversal of sign in the Young's moduli, which essentially reverses the state (compression or tension) of deformation under an applied external mechanical stress. For clarity, we show the numerical results related to positive and negative Young's moduli using two separate subplots in Figures 10 – 14. In all the figures arrows (red and blue color) have been used for depicting the increase in voltage (V) at a constant stress and increase in stress (Pa) at constant voltage respectively.

In order to determine the sign for $\bar{E}_1$ and $\bar{E}_2$, the sign and magnitude of A_{uni}, A_{Bi}, B_{uni} and B_{Bi} as mentioned in Equations (59), (61), (69) and (71) plays a vital role. The dependency of these parameters on d_{31}, voltage and cell angle can be understood from the Table 2. Here A_{uni} and A_{Bi} depends on all the parameters which are mentioned in the Table 2, while B_{uni} and B_{Bi}, both are independent of the sign of cell angle. Thus, voltage, plays an important role in determining the sign for $\bar{E}_2$. However, investigating the signs alone is not enough, magnitude also plays a major role as explained in the Fig. 9. $\bar{E}_1$ and $\bar{E}_2$ become negative only when the respective parameters among A_{uni}, A_{Bi}, B_{uni} and B_{Bi} assume a value less than –1.

The Young's moduli become undefined if the respective numerical value among A_{uni}, A_{Bi}, B_{uni} and B_{Bi} goes to –1 in Equations (59), (61), (69) and (71). Equating equations for A_{uni}, A_{Bi}, B_{uni} and B_{Bi} to -1, we can write the following equations.

$$\sin^2 \theta_{uni}^{E_1} + \frac{h}{L} \sin \theta_{uni}^{E_1} + \frac{3V(1+\alpha)d_{31}Y_p}{\sigma_1 L} \frac{T_s}{L} = 0 \tag{84}$$

$$\sin^2 \theta_{Bi}^{E_1} + \frac{h}{L} \sin \theta_{Bi}^{E_1} + \frac{6V(1+\alpha)d_{31}Y_p}{\sigma_1 L} \frac{T_s}{L} = 0 \tag{85}$$

Table 3: For different combinations of voltage and stress values, critical angle (θ_{CR}) is presented. Also, the ($V \setminus \sigma$) ratio required to programme the transition from positive Young's modulus to negative Young's modulus and vice versa is mentioned (If the ratio of voltage to sigma for a particular instance is more than the respective ratio mentioned in the table for the VD case, then the Young's moduli plots appear entirely in one quadrant (either in negative or positive). In case of SD, however, it is not possible to have Young's modulus in one quadrant unless we assign voltage equals to zero or negative (for E_2 only). Even for a very small value of voltage, the transition takes place, but the range of cell angle, in which the Young's modulus is negative, becomes small.).

Configurations	V and σ	Critical angle (θ_{CR})	($V \setminus \sigma$) ratio to eliminate transisition
$\bar{E}_1$ Unimorph (VD)	V = 70, σ = 60 Pa	48.43019	$\frac{V}{\sigma} = \frac{100.819}{60} = 1.68$
	V =-70, σ= 60 Pa	Not Defined	$\frac{V}{\sigma} = \frac{-43.208}{60} = $ -0.7201
$\bar{E}_1$ Bimorph (VD)	V = 70, σ = 60 Pa	55.362	$\frac{V}{\sigma} = \frac{89.61}{60} = 1.4935$
	V = -70, σ = 60 Pa	Not Defined	$\frac{V}{\sigma} = \frac{-38.4072}{60} = $ -0.64012
$\bar{E}_2$ Unimorph (VD)	V = 40, σ= 120 Pa	$\pm$ 33.5654	$\frac{V}{\sigma} = \frac{57.61}{120} = 0.48$
	V =-40, σ= 120 Pa	Not Defined	NA
$\bar{E}_2$ Bimorph (VD)	V = 40, σ= 120 Pa	$\pm$ 27.8952	$\frac{V}{\sigma} = \frac{51.209}{120} = 0.4267$
	V = -40, σ = 120 Pa	Not Defined	NA
$\bar{E}_1$ Unimorph (SD)	V = 100, σ = 1000 Pa	4.6294	$\frac{V}{\sigma} = 0$
	V = -100, σ = 1000 Pa	-4.95057	$\frac{V}{\sigma} = 0$
$\bar{E}_1$ Bimorph (SD)	V = 100, σ = 1000 Pa	5.19	$\frac{V}{\sigma} = 0$
	V = -100, σ = 1000 Pa	-5.5973	$\frac{V}{\sigma} = 0$
$\bar{E}_2$ Unimorph (SD)	V = 40, σ = 1000 Pa	$\pm$ 73.2229	$\frac{V}{\sigma} = 0$
	V = -40, σ = 1000 Pa	Not Defined	NA
$\bar{E}_2$ Bimorph (SD)	V = 40, σ = 1000 Pa	$\pm$ 72.1722	$\frac{V}{\sigma} = 0$
	V = -40, σ = 1000 Pa	Not Defined	NA

$$\cos^2 \theta_{uni}^{E_2} = \frac{-3 d_{31} Y_p V (1 + \alpha)}{\sigma_2 L} \frac{T_s}{L} \tag{86}$$

$$\cos^2 \theta_{Bi}^{E_2} = \frac{-6 d_{31} Y_p V (1 + \alpha)}{\sigma_2 L} \frac{T_s}{L} \tag{87}$$

(a) Unimorph: Positive Voltage

(b) Unimorph: Negative Voltage

(c) Bimorph: Positive Voltage
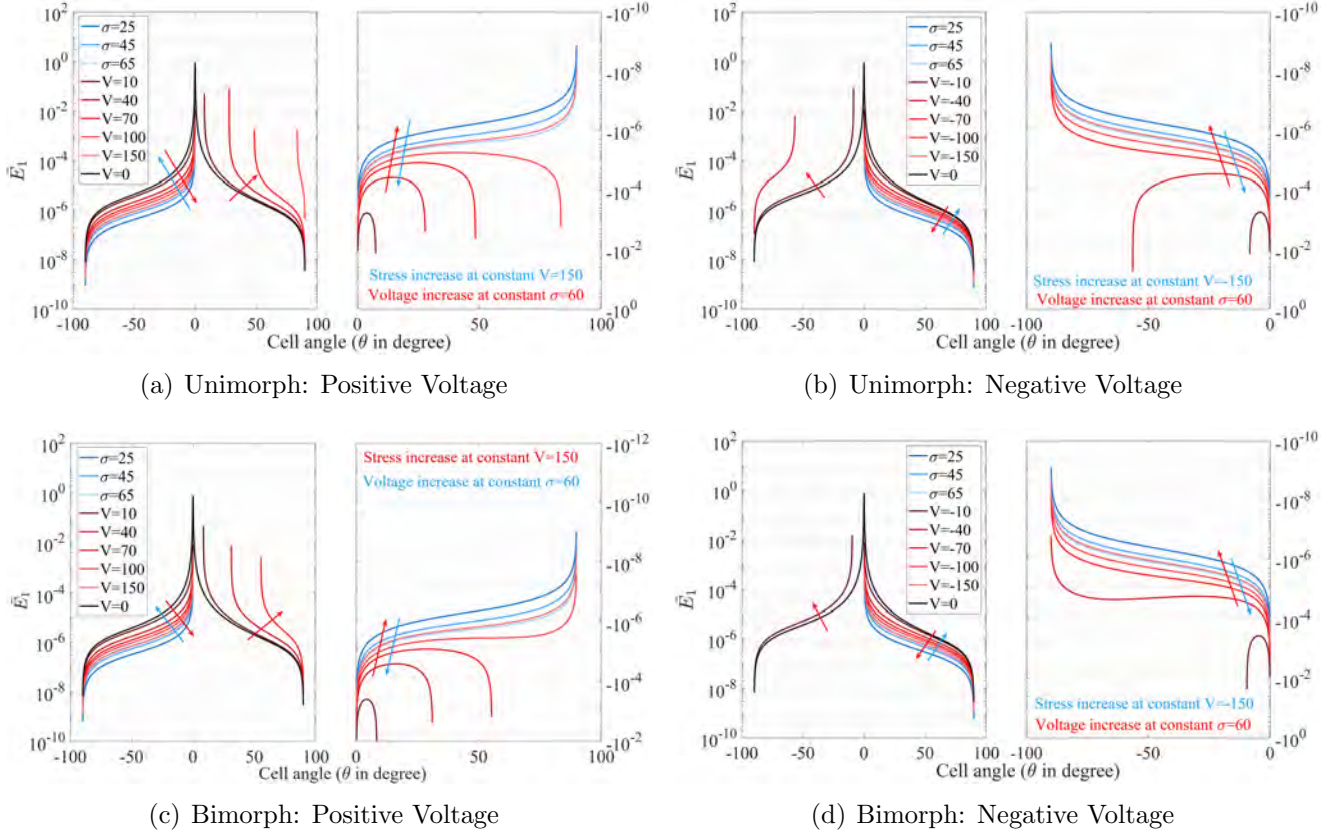
(d) Bimorph: Negative Voltage

Fig. 10: Variation of $\bar{E}_1$ ($= E_1 \setminus Y_s$) for unimorph/ bimorph configuration under positive/ negative applied voltage (voltage dominant) at a constant stress and under varying stress at a constant voltage with the change in cell angle. In each plot, the left subplot has Young's modulus with positive sign whereas, in the right subplot it has negative sign. Here, the arrows depict the increase in voltage (V) at a constant stress (red color) and increase in stress (Pa) at constant voltage (blue color). The legend is valid for all the subplots.

For a specific combination of voltage and stress, the values of $\theta_{uni}^{E_1}$, $\theta_{Bi}^{E_1}$, $\theta_{uni}^{E_2}$, $\theta_{Bi}^{E_2}$ (which are termed as critical angle) are calculated as shown in *Table* 3. At these critical values of cell angle, as given by the above equations, $\bar{E}_1$ and $\bar{E}_2$ are undefined for unimorph and bimorph configurations. A transition from negative to positive Young's modulus also occurs at these critical angle values. Representative numerical results for critical angle values obtained using the above expressions with the change in voltage and stress values are given in the Table 3. In addition to this, the $(V \setminus \sigma)$ ratio in Table 3 helps to predict the trend of voltage-dependent Young's moduli plots including change in sign. If the ratio of voltage to sigma for a particular instance is more than the ratio mentioned in the table for the VD case, then the Young's moduli plots appear entirely in one quadrant (either in left or right subplot for the respective case). In case of SD, however, it is not possible to have Young's modulus in one quadrant unless we assign voltage equals to zero or negative (for E_2 only). Even for a very small value of voltage, the transition takes place, but the range of cell angle, in which the Young's modulus is negative, becomes small.

For the voltage dominant case, variation in $\bar{E}_1$ with cell angle as a function of the voltage and applied stress (σ_1) is shown in Fig. 10. In the voltage dominant (VD) case the sign of Young's modulus for most of the range of cell angle is determined by change in voltage. From Fig. 10, it can be observed that when the voltage is zero, the Young's modulus is positive for all cell angle. When the value of A_{uni} and A_{Bi} are greater than 0, then the Young's modulus decreases with the increase in voltage (refer to 10(a) and 10(c) for positive cell angle, while 10(b) and 10(d) for
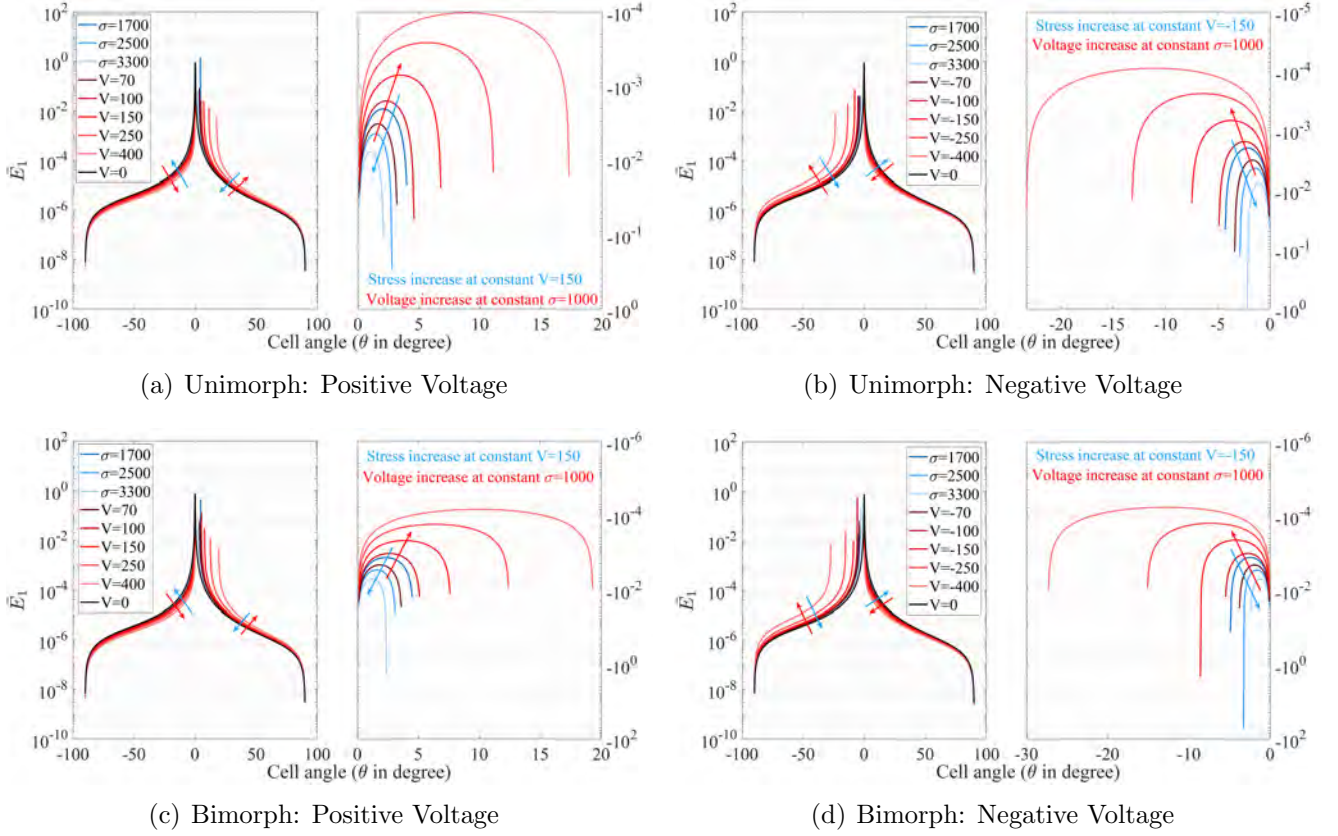
(a) Unimorph: Positive Voltage

(b) Unimorph: Negative Voltage

(c) Bimorph: Positive Voltage

(d) Bimorph: Negative Voltage

Fig. 11: Variation of $\bar{E}_1$ ($= E_1 \setminus Y_s$) for unimorph/ bimorph configuration under positive/ negative applied voltage (stress dominant) at a constant stress, and under varying stress at a constant voltage with the change in cell angle. In each plot, the left subplot has Young's modulus with positive sign, whereas in the right subplot it has negative sign. Here, the arrows depict the increase in voltage (V) at a constant stress (red color) and increase in stress (Pa) at constant voltage (blue color). The legend is valid for all the subplots.
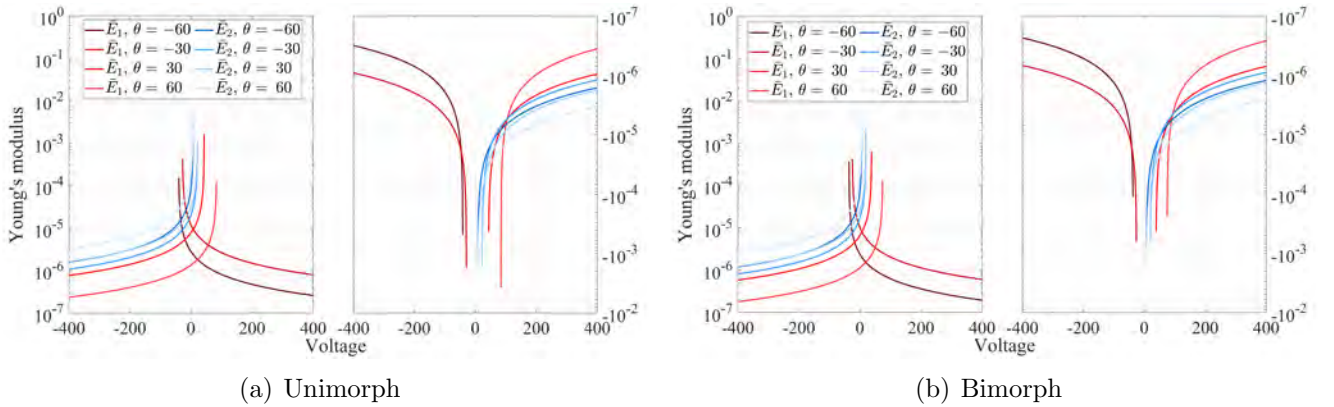

(a) Unimorph

(b) Bimorph

Fig. 12: Variation of $\bar{E}_1$ ($= E_1 \setminus Y_s$) and $\bar{E}_2$ ($= E_2 \setminus Y_s$) with voltage (V) for different cell angle ($-30°$, $-60°$, $30°$, $60°$) at constant stress ($\sigma = 60$ Pa) and constant $h \setminus L$ ratio $= 2.5$. In each plot, the left subplot has Young's modulus with positive sign, whereas in the right subplot sign of Young's modulus is negative. Here, the legend is valid for all the subplots.

negative cell angle). For positive cell angle in the Figures as mentioned above, when the values A_{uni} and A_{Bi} are less than -1 and beyond a critical voltage as mentioned in Table 3, the value of Young's modulus is found to be entirely negative. The fluctuations in the Young's modulus occur
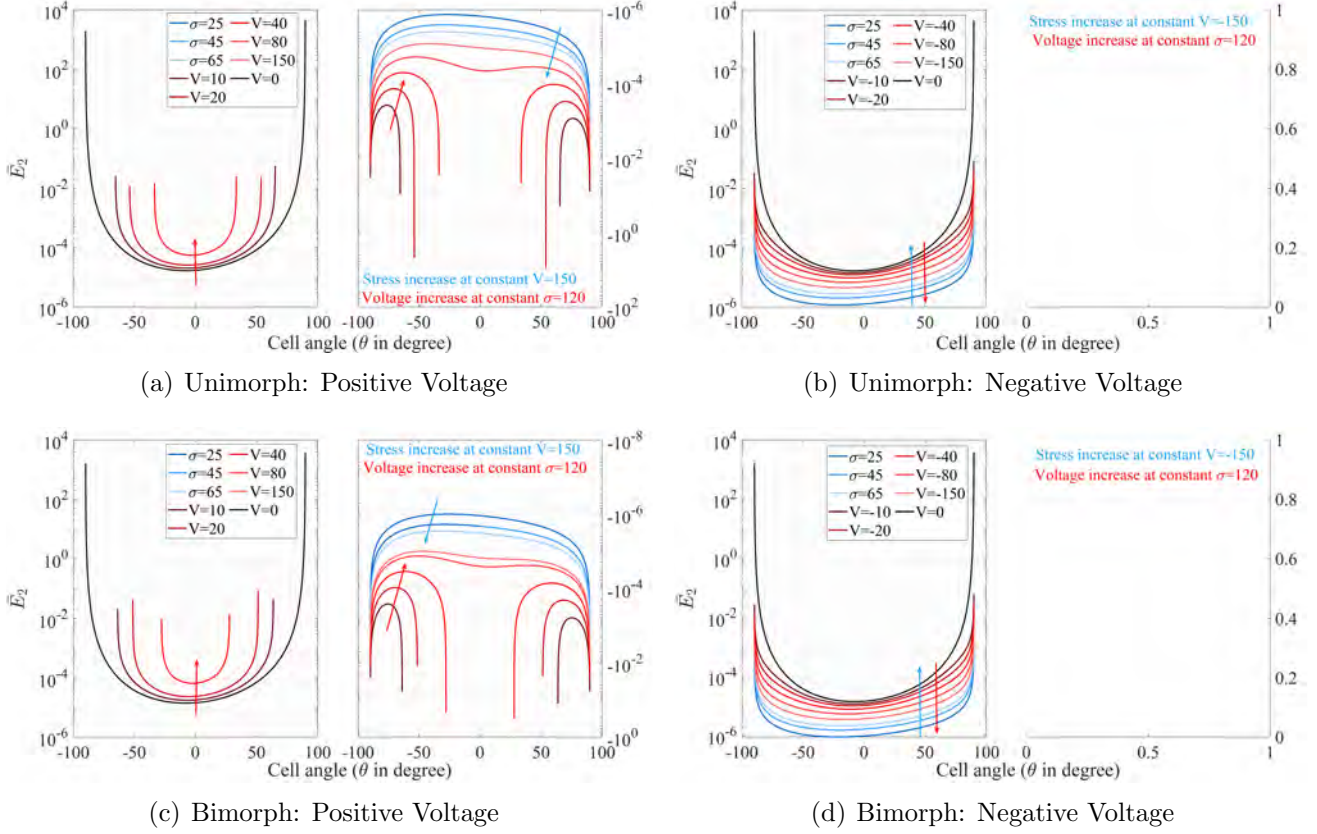
Fig. 13: Variation of $\bar{E}_2 \, (= E_2 \setminus Y_s)$ for unimorph/ bimorph configuration under positive/ negative applied voltage (voltage dominant) at a constant stress, and under varying stress at a constant voltage with the change in cell angle. In each plot, the left subplot has Young's modulus with positive sign whereas, in the right subplot it has negative sign. Here, the arrows depict the increase in voltage (V) at a constant stress (red color) and increase in stress (Pa) at constant voltage (blue color). The legend is valid for all the subplots.

at critical angle when the value of A_{uni} and A_{Bi} varies in the range of 1 to –1. The variation of the properties for $\bar{E}_1$ has been summarised in Table 4.

Fig. 11 shows the numerical results concerning $\bar{E}_1$ for the stress dominant (SD) case, wherein the value of stress dominates the sign of Young's modulus for majority of cell angle. Here the effect of stress is much higher compared to that of voltage. Thus, for most of the cell angle, the Young's modulus is positive as the value of A_{uni} and A_{Bi} is less than 1 irrespective of the sign which changes due to cell angle and voltage. For low voltages, the transition angle is close to 5°, but for a high voltage (say 400V), it is close to 15°, as shown in Fig. 11. In order to avoid the transition in SD case (i.e. for keeping Young's modulus in one quadrant only), the voltage has to be zero, and there is no other possible option, in which the transition can be avoided. Furthermore, the change in the sign of Young's modulus can be observed when the value of stress is increased, and voltage is kept constant. When the value of $(1+A_{uni})$ or $(1+A_{Bi})$ increases, the Young's modulus decreases and vice versa.

Fig. 12 shows the variation of $\bar{E}_1$ and $\bar{E}_2$ with voltage considering different non-auxetic and auxetic cellular configurations. From the figure, it becomes evident that the sign of $\bar{E}_2$ is independent of cell angle. The sign of $\bar{E}_2$ only changes because of variation in voltage. However, for $\bar{E}_1$, it can be observed that, along with voltage, cell angle also plays an important role in determining the sign. The dependency of the $\bar{E}_2$ on voltage for different cases namely, voltage dominant (positive and negative voltage) and stress dominant (positive and negative voltage), are plotted in Fig. 13
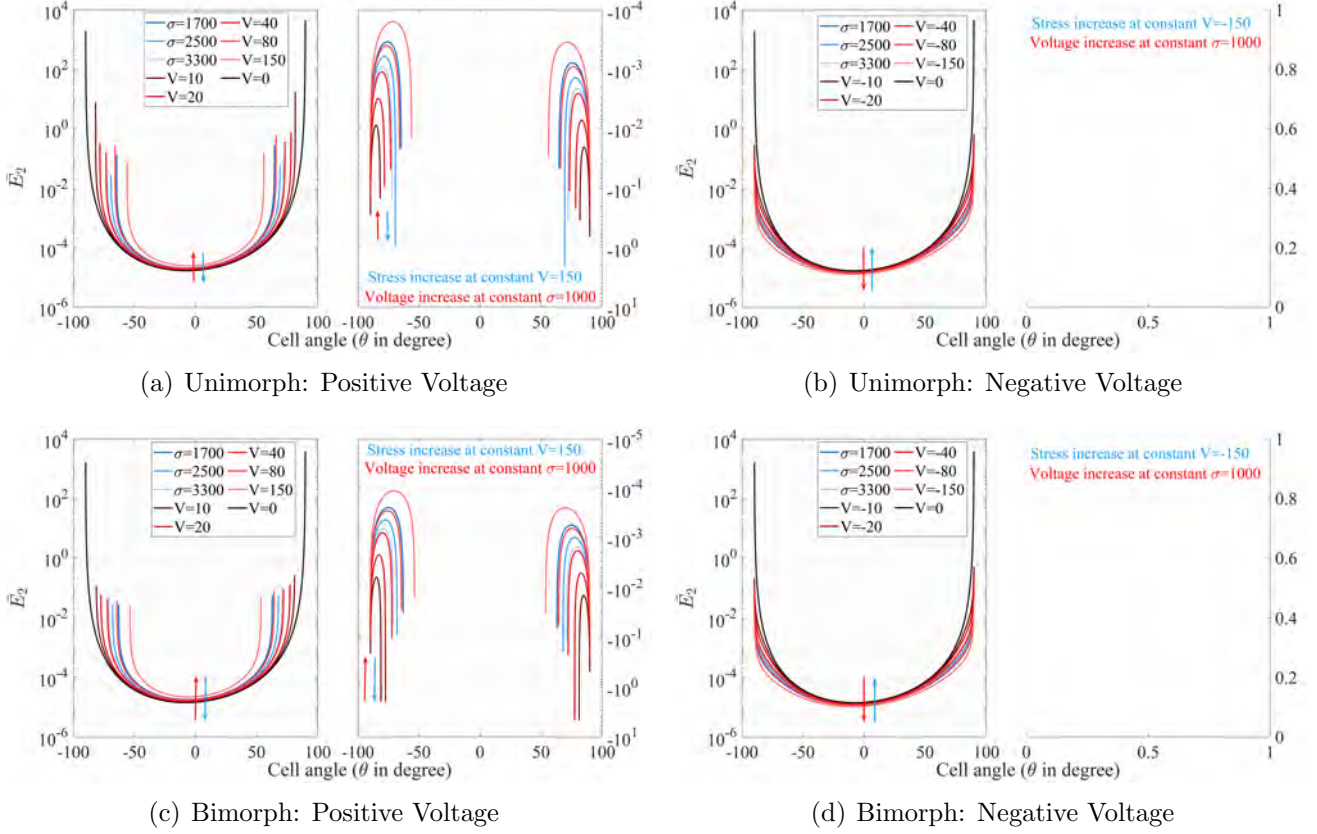
Fig. 14: Variation of $\bar{E}_2$ $(= E_2 \setminus Y_s)$ for unimorph/ bimorph configuration under positive/ negative applied voltage (stress dominant) at a constant stress, and under varying stress at a constant voltage with the change in cell angle. In each plot, the left subplot has Young's modulus with positive sign, whereas the right subplot has negative sign. Here, the arrows depict the increase in voltage (V) at a constant stress (red color) and increase in stress (Pa) at constant voltage (blue color). The legend is valid for all the subplots.

and Fig. 14. The plots can be explained by referring to the Equations (69) and (71), where B_{uni} and B_{Bi} are found to be independent of the signs of cell angle as discussed earlier. For the VD case, value of externally applied stress is much lesser compared to the applied voltage. When the applied voltage is positive, and the magnitudes of B_{uni} and B_{Bi} are greater than 1, then the value of Young's modulus is always negative if the sign for B_{uni} and B_{Bi} is negative as shown in Figures 13(a), 13(c), 14(a) and 14(c). The transition could occur when the values of B_{uni} and B_{Bi} are just less than –1. This occurs at some specific values of critical angle. Representative such values of critical angle for some of the voltages are given in Table 3. When the applied voltage is negative, the sign of Young's modulus depends on two factors, the magnitude and sign of B_{uni} and B_{Bi}. If the sign of B_{uni} and B_{Bi} is positive then magnitude will not matter and the Young's modulus will be always positive. In another scenario, if the sign of B_{uni} and B_{Bi} is negative then magnitude plays very important role i.e. if the magnitude is less than 1 but greater than 0 then sign of Young's modulus will be positive and if the magnitude is greater than 1 then sign will always be negative for all the values of voltage and stress. So, due to this reason when the voltage is negative, right subplots in Figure 13(b), 13(d), 14(b) and 14(d) are empty. Moreover, with the increase in voltage the value of B_{uni} and B_{Bi} increases, which leads to decrease in the value of Young's modulus as shown in Figures 13(b), 13(d), 14(b) and 14(d). For the SD case, when a positive voltage is applied, transition from negative Young's modulus to positive Young's modulus can be observed in 14(a) and 14(c), while for a negative applied voltage, Young's modulus is positive

for every cell angle as shown in 14(b) and 14(d). For both VD and SD, when a negative voltage is applied, the values of B_{uni} and B_{Bi} are positive and we get only positive Young's modulus. When only applied stress is increased by keeping the voltage constant, the value of Young's modulus increases for negative voltage only. Summary of the results are discussed in the following section for all the possible cases.

4.3. Summary

The major observations on the trends of numerical results presented in the preceding subsections are summarised here under voltage dominant (VD) and stress dominant (SD) environments (refer to Table 4).

- For $\bar{E}_1$ VD/SD case (unimorph/ bimorph), the Young's modulus increases with increase in voltage under two conditions, positive cell angle and positive voltage, or negative cell angle and negative voltage. A reverse trend is noticed for any other combination.

- For $\bar{E}_1$ VD/SD case (unimorph/ bimorph), when the value of stress has increased the value of Young's modulus increases for these two cases only when voltage is positive, and cell angle is negative and when cell angle is positive, and voltage is negative. For all other cases, the value of Young's modulus decreases.

- For $\bar{E}_2$ VD/SD case (unimorph/ bimorph), when the value of voltage is increased, Young's modulus increases under only one condition, i.e., when the applied voltage is positive. Transverse Young's modulus is independent of the sign of cell angle. When a negative voltage is applied, value of Young's modulus decreases as the voltage increases and the variation is restricted in one subplot only.

- For $\bar{E}_2$ VD/SD case (unimorph/ bimorph), when the value of stress is increased, the value of Young's modulus increases if the value of applied voltage is negative and is contained in one subplot. However, on the other hand, as the positive voltage is increased, the value of Young's modulus decreases.

Table 4: General trends of Young's moduli for unimorph (Uni) and bimorph (Bi) configurations under the variation of different influencing parameters. Here, ↑ and ↓ denote the increase and decrease for the respective parameters.

Modulus	Voltage dominant/Stress dominant							
	Positive Voltage				Negative Voltage			
	θ: Positive		θ: Negative		θ: Positive		θ: Negative	
	V ↑	σ ↑	V ↑	σ ↑	V ↑	σ ↑	V ↑	σ ↑
$\bar{E}_1$ (Uni)	↑	↓	↓	↑	↓	↑	↑	↓
$\bar{E}_1$ (Bi)	↑	↓	↓	↑	↓	↑	↑	↓
$\bar{E}_2$ (Uni)	↑	↓	↑	↓	↓	↑	↓	↑
$\bar{E}_2$ (Bi)	↑	↓	↑	↓	↓	↑	↓	↑

5. Conclusions and perspective

We have proposed a hybrid piezo-embedded lattice material microstructure, where the Young's moduli can be actively programmed as a function of applied electrical field. Normally effective elastic properties of lattices are passive in nature and functions of the microstructural geometry and

intrinsic material properties. It is not possible to modulate the elastic properties of such traditional lattices actively after manufacturing. The current proposition on hybrid piezo-embedded lattices essentially implies that it will be possible to program the effective Young's moduli of materials based on operational demands using externally applied electrical field. This will lead to the development of futuristic optimal structural systems where the mechanical properties of the system could be actively interfaced with the surrounding environments and operational conditions.

A bottom-up analytical framework for the elastic moduli of active lattices leading to closed-form expressions is presented in this article, wherein it is revealed that the two Young's moduli depend on the applied electrical field. Other in-plane elastic properties like shear modulus and Poisson's ratios of the proposed hybrid microstructure are not dependent on the applied electrical field. On the contrary to conventional notion of elastic moduli for linear small-scale deformation, we for the first time, show that the Young's moduli can become stress-dependent under non-zero applied voltage.

An intriguing outcome of this article is that the compound interaction between electrical field and applied mechanical stress could lead to unusual negative values of elastic moduli for the proposed lattice. Though negative Young's moduli in lattice materials have been reported under dynamic conditions before, this is the first instance where we demonstrate that the Young's moduli could become negative in static condition when an external electrical field is applied. The parameter space for effective negative Young's modulus is found to depend on certain material and geometric attributes of the lattice microstructure as well as the external electrical field and applied stress in a unique manner, which is numerically characterised as an integral part of this investigation. It is shown that a programmable state-transition of Young's moduli can be achieved based on the active parameter space. Although we have concentrated on hexagonal lattices in this paper, the proposed analytical framework is generic in nature and could be extended to other lattices in two and three dimensions. In essence, the investigation presented in this article concerning voltage-dependent active modulation of elastic properties including the possibility of reversal in their nature would significantly contribute to the development of futuristic optimal material microstructures at multiple length scales for exploiting the new dimensions of active on-demand modulation of elastic moduli unravelled in terms electrical field.

References

Adhikari, S., Mukhopadhyay, T., Shaw, A., Lavery, N., 2020. Apparent negative values of young's moduli of lattice materials under dynamic conditions. International Journal of Engineering Science 150, 103231.

Balawi, S., Abot, J. L., AUG 2008. The effect of honeycomb relative density on its effective in-plane elastic moduli: An experimental study. Composite Structures 84 (4), 293–299.

Chen, C., Lu, T., Fleck, N., NOV 1999. Effect of imperfections on the yielding of two-dimensional foams. Journal of the Mechanics and Physics of Solids 47 (11), 2235–2272.

Chen, Y., Li, T., Scarpa, F., Wang, L., Feb 2017. Lattice metamaterials with mechanically tunable poisson's ratio for vibration control. Phys. Rev. Applied 7, 024012.

Chopra, I., Sirohi, J., 2013. Smart Structures Theory. Cambridge Aerospace Series. Cambridge University Press.

Crawley, E. F., Anderson, E. H., 1990. Detailed models of piezoceramic actuation of beams. Journal of Intelligent Material Systems and Structures 1 (1), 4–25.

Crawley, E. F., de Luist, J., 1987. Use of piezoelectric actuators as elements of intelligent structures. American Institute of Aeronautics and Astronautics Journal 25 (10), 1373–1385.

Dwivedi, A., Banerjee, A., Bhattacharya, B., 2020. Simultaneous energy harvesting and vibration attenuation in piezo-embedded negative stiffness metamaterial. Journal of Intelligent Material Systems and Structures 31 (8), 1076–1090.

El-Sayed, F. A., Jones, R., Burgess, I., 1979. A theoretical approach to the deformation of honeycomb based composite materials. Composites 10 (4), 209 – 214.

Erturk, A., Inman, D., 2011. Piezoelectric Energy Harvesting. John Wiley & Sons, Ltd, pp. 151–157.

Gibson, L., Ashby, M. F., 1999. Cellular Solids Structure and Properties. Cambridge University Press, Cambridge, UK.

Grima, J. N., Attard, D., Ellul, B., Gatt, R., 2011. An Improved Analytical Model for the Elastic Constants of Auxetic and Conventional Hexagonal Honeycombs. Cellular Polymers 30 (6), 287–310.

Harkati, A., Boutagouga, D., Harkati, E., Bezazi, A., Scarpa, F., Ouisse, M., 2020. In-plane elastic constants of a new curved cell walls honeycomb concept. Thin-Walled Structures 149, 106613.

Iyer, S., Alkhader, M., Venkatesh, T., 2016. On the relationships between cellular structure, deformation modes and electromechanical properties of piezoelectric cellular solids. International Journal of Solids and Structures 80, 73 – 83.

Jang, W.-Y., Kyriakides, S., 2015. On the buckling and crushing of expanded honeycomb. International Journal of Mechanical Sciences 91, 81 – 90.

Lee, D. G., Or, S. W., Carman, G. P., 2004. Design of a piezoelectric-hydraulic pump with active valves. Journal of Intelligent Material Systems and Structures 15 (2), 107–115.

Li, Y., Baker, E., Reissman, T., Sun, C., Liu, W. K., 2017. Design of mechanical metamaterials for simultaneous vibration isolation and energy harvesting. Applied Physics Letters 111 (25), 251903.

Malek, S., Gibson, L., 2015. Effective elastic properties of periodic hexagonal honeycombs. Mechanics of Materials 91, 226 – 240.

Mukhopadhyay, T., Adhikari, S., 2016a. Effective in-plane elastic properties of auxetic honeycombs with spatial irregularity. Mechanics of Materials 95, 204 – 222.

Mukhopadhyay, T., Adhikari, S., 2016b. Equivalent in-plane elastic properties of irregular honeycombs: An analytical approach. International Journal of Solids and Structures 91, 169 – 184.

Mukhopadhyay, T., Adhikari, S., 2016c. Free vibration analysis of sandwich panels with randomly irregular honeycomb core. Journal of Engineering Mechanics 142, 06016008.

Mukhopadhyay, T., Adhikari, S., 2017a. Effective in-plane elastic moduli of quasi-random spatially irregular hexagonal lattices. International Journal of Engineering Science 119, 142 – 179.

Mukhopadhyay, T., Adhikari, S., 2017b. Stochastic mechanics of metamaterials. Composite Structures 162, 85 – 97.

Mukhopadhyay, T., Adhikari, S., Alu, A., 2019a. Probing the frequency-dependent elastic moduli of lattice materials. Acta Materialia 165, 654 – 665.

Mukhopadhyay, T., Adhikari, S., Alu, A., 2019b. Theoretical limits for negative elastic moduli in subacoustic lattice materials. Phys. Rev. B 99, 094108.

Mukhopadhyay, T., Adhikari, S., Batou, A., 2019c. Frequency domain homogenization for the viscoelastic properties of spatially correlated quasi-periodic lattices. International Journal of Mechanical Sciences 150, 784 – 806.

Mukhopadhyay, T., Ma, J., Feng, H., Hou, D., Gattas, J. M., Chen, Y., You, Z., 2020a. Programmable stiffness and shape modulation in origami materials: Emergence of a distant actuation feature. Applied Materials Today 19, 100537.

Mukhopadhyay, T., Mahata, A., Adhikari, S., Zaeem, M. A., 2017a. Effective elastic properties of two dimensional multiplanar hexagonal nano-structures. 2D Materials 4, 025006.

Mukhopadhyay, T., Mahata, A., Adhikari, S., Zaeem, M. A., 2017b. Effective mechanical properties of multilayer nano-heterostructures. Scientific Reports 7, 15818.

Mukhopadhyay, T., Mahata, A., Naskar, S., Adhikari, S., 2020b. Probing the effective young's modulus of 'magic angle' inspired multi-functional twisted nano-heterostructures. Advanced Theory and Simulations 3, 2000129.

Mukhopadhyay, T., Naskar, S., Adhikari, S., 2020c. Anisotropy tailoring in geometrically isotropic multi-material lattices. Extreme Mechanics Letters 40, 100934.

Rapaka, S. D., Pandey, M., Annabattula, R. K., 2020. Effect of defects on the dynamic compressive behavior of cellular solids. International Journal of Mechanical Sciences 170, 105365.

Roark, R. J., Young, W. C., 1976. Formulas for Stress and Strain. McGraw-Hill Book Company.

Ryvkin, M., Shraga, R., 2018. Fracture toughness of hierarchical self-similar honeycombs. International Journal of Solids and Structures 152-153, 151 – 160.

Scarpa, F., Panayiotou, P., Tomlinson, G., SEP 2000. Numerical and experimental uniaxial loading on in-plane

auxetic honeycombs. Journal Of Strain Analysis for Engineering Design 35 (5), 383–388.

Silva, M., Gibson, L., MAY 1997. The effects of non-periodic microstructure and defects on the compressive strength of two-dimensional cellular solids. International Journal of Mechanical Sciences 39 (5), 549–563.

Silva, M., Hayes, W., Gibson, L., NOV 1995. The effects of non-periodic microstructure on the elastic properties of 2-dimensional cellular solids. International Journal of Mechanical Sciences 37 (11), 1161–1177.

Sorohan, S., Constantinescu, D. M., Sandu, M., Sandu, A. G., 2019. In-plane homogenization of commercial hexagonal honeycombs considering the cell wall curvature and adhesive layer influence. International Journal of Solids and Structures 156-157, 87 – 106.

Thomas, T., Tiwari, G., 2019. Energy absorption and in-plane crushing behavior of aluminium reinforced honeycomb. Vacuum 166, 364 – 369.

Wang, A., McDowell, D., NOV 2003. Effects of defects on in-plane properties of periodic metal honeycombs. International Journal of Mechanical Sciences 45 (11), 1799–1813.

Wang, H., Zhao, D., Jin, Y., Wang, M., Mukhopadhyay, T., You, Z., 2020. Modulation of multi-directional auxeticity in hybrid origami metamaterials. Applied Materials Today 20, 100715.

Wei, L., Zhao, X., Yu, Q., Zhu, G., 2020. A novel star auxetic honeycomb with enhanced in-plane crushing strength. Thin-Walled Structures 149, 106623.

Wilbert, A., Jang, W., Kyriakides, S., Floccari, J., 2011. Buckling and progressive crushing of laterally loaded honeycomb. International Journal of Solids and Structures 48 (5), 803 – 816.

Zenkert, D., 1995. An introduction to sandwich construction. Cradley Heath, Warley: Engineering Materials Advisory Services.

Zhang, J., Ashby, M., 1992. The out-of-plane properties of honeycombs. International Journal of Mechanical Sciences 34 (6), 475 – 489.

Zhang, Y., Qiu, X., Fang, D., 2008. Mechanical properties of two novel planar lattice structures. International Journal of Solids and Structures 45 (13), 3751 – 3768.

Zhao, Y., Ge, M., Ma, W., 2020. The effective in-plane elastic properties of hexagonal honeycombs with consideration for geometric nonlinearity. Composite Structures 234, 111749.

Zhu, H., Hobdell, J., Windle, A., 2001. Effects of cell irregularity on the elastic properties of 2d voronoi honeycombs. Journal of the Mechanics and Physics of Solids 49 (4), 857 – 870.